Gas Separation Hot Paper

International Edition: DOI: 10.1002/anie.201809869
German Edition: DOI: 10.1002/ange.201809869

A Metal–Organic Framework with Suitable Pore Size and Specific Functional Sites for the Removal of Trace Propyne from Propylene

Libo Li, Hui-Min Wen, Chaohui He, Rui-Biao Lin, Rajamani Krishna, Hui Wu, Wei Zhou, Jinping Li, Bin Li, and Banglin Chen**

Abstract: *Separation of propyne/propylene (C_3H_4/C_3H_6) is more difficult and challenging than that of acetylene/ethylene (C_2H_2/C_2H_4) because of their closer molecular sizes. A comprehensive screening of a series of metal–organic frameworks with broad types of structures, pore sizes, and functionalities was carried out. UTSA-200 was identified as the best separating material for the removal of trace C_3H_4 from C_3H_4/C_3H_6 mixtures. Gas sorption isotherms reveal that UTSA-200 exhibits by far the highest C_3H_4 adsorption capacity (95 $cm^3 cm^{-3}$ at 0.01 bar and 298 K) and record C_3H_4/C_3H_6 selectivity, which was mainly attributed to the suitable dynamic pore size to efficiently block the larger C_3H_6 molecule whilst the strong binding sites and pore flexibility capture smaller C_3H_4. This material thus provides record purification capacity for the removal of C_3H_4 from a 1:99 (or 0.1:99.9, v/v) C_3H_4/C_3H_6 mixture to produce 99.9999 % pure C_3H_6 with a productivity of 62.0 (or 142.8) mmol g^{-1}.*

Adsorptive separation based on porous materials opens the door to enable a possible transition from traditional energy-intensive cryogenic distillation to the energy-efficient adsorbent-based separation for industrial gas separation and purification.[1] Compared to conventional activated carbons and zeolites, the emerging microporous metal–organic frameworks (MOFs) have attracted immense attention for gas separation/purification in recent years owing to their fascinating tunability with respect to pore size, shape, and surface functionality.[2] These features have enabled us to design target materials with the on-demand pore size and functionality for diverse gas separation and purification, including separation of CO_2/N_2, CO_2/CH_4, light hydrocarbons, C_2H_2/CO_2, O_2/N_2, CO/CO_2, and so on.[3]

Gas molecules with quite different molecular weights and thus vapor pressures or boiling points, for example, CO_2 and N_2, can be easily separated because of their different interactions with porous materials.[4] Those gas molecules with similar molecular weights and vapor pressures are difficult and challenging to be separated.[5] Ultramicroporous MOFs are superior to well-developed porous materials for gas separation/purification; this superiority is attributed to their power of the finely tuned pores to enforce the sieving effects and the readily immobilized functional sites on the pore surfaces to introduce the specific recognition with one of the gas molecules, and the interplay of dual functionalities of both the suitable size and functional site.[6,7] Indeed, a few ultramicroporous MOFs have been discovered for the very challenging separations of C_2H_2/C_2H_4, C_2H_2/CO_2, C_2H_4/C_2H_6, and C_3H_4/C_3H_6 over the past several years.[7] Compared with the separation of C_2H_2/C_2H_4, the C_3H_4/C_3H_6 separation is more difficult and challenging. As shown in Scheme 1, acetylene and ethylene are the simplest alkyne and alkene with a three-dimensional (3D) size of $3.32 \times 3.34 \times 5.70$ and $3.28 \times 4.18 \times 4.84$ Å^3, respectively. The kinetic diameter difference between C_2H_2 (3.3 Å) and C_2H_4 (4.2 Å) is about 0.9 Å.[8] Propyne and propylene, also known as methylacetylene and

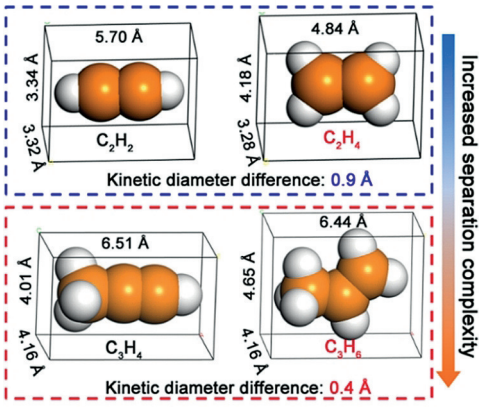

Scheme 1. Comparison of molecular size and kinetic diameter difference of C_2H_2/C_2H_4 and C_3H_4/C_3H_6.

[*] Dr. L. Li, C. He, Prof. J. Li
College of Chemistry and Chemical Engineering
Taiyuan University of Technology
Taiyuan 030024, Shanxi (China)
Dr. L. Li, Dr. R.-B. Lin, Prof. B. Chen
Department of Chemistry, University of Texas at San Antonio
One UTSA Circle, San Antonio, TX 78249-0698 (USA)
E-mail: banglin.chen@utsa.edu
Prof. B. Li
State Key Laboratory of Silicon Materials
School of Materials Science and Engineering, Zhejiang University
Hangzhou 310027 (China)
E-mail: bin.li@zju.edu.cn
Dr. H.-M. Wen
College of Chemical Engineering, Zhejiang University of Technology
Zhejiang, 310014 (China)
Prof. R. Krishna
Van't Hoff Institute for Molecular Sciences, University of Amsterdam
Science Park 904, 1098 XH Amsterdam (The Netherlands)
Dr. H. Wu, Dr. W. Zhou
NIST Center for Neutron Research
National Institute of Standards and Technology
Gaithersburg, MD 20899-6102 (USA)
Supporting information and the ORCID identification number(s) for the author(s) of this article can be found under: https://doi.org/10.1002/anie.201809869.

methylethylene, have a larger size of $4.16 \times 4.01 \times 6.51$ and $4.65 \times 4.16 \times 6.44$ Å^3. C_3H_4 is a linear molecule, and C_3H_6 has a curved shape. Despite different shapes, the relatively bulky methyl group makes the kinetic diameter difference between the pair C_3H_4 and C_3H_6 (4.2 and 4.6 Å) much closer (nearly 0.4 Å) than C_2H_2/C_2H_4.[2a] The smaller the size difference between the pair of molecules is, the more difficult the separation will be.

Removal of trace C_3H_4 (1000 or 10000 ppm) from C_3H_4/C_3H_6 mixtures is one of the most important separation processes to produce polymer-grade C_3H_6 gas (the C_3H_4 impurity should be lower than 5 ppm), a prime olefin raw material for petrochemical production. Microporous materials for C_3H_4/C_3H_6 separation have not been well-explored, with only the ELM-12, SIFSIX-3-Ni (SIFSIX = hexafluorosilicate (SiF_6^{2-})) and ZU-62 having been reported.[9] While these materials exhibit high C_3H_4 adsorption capacity, they only exhibit moderately high gas-separation performance because of the comparatively large pores to include both C_3H_4 and C_3H_6 molecules, thus limiting the productivity of the desired C_3H_6 product. Targeting high performance porous materials can not only significantly enhance the C_3H_6 productivity, but also increase the purity of the C_3H_6 product, thus reduce the energy cost for this important industrial separation. Adsorption selectivity and uptake capacity are the two most important criteria that are directly related to productivity and purity, but it is very difficult to target materials with both high values (so-called trade-off). To realize high selectivity and adsorption uptake simultaneously, ideal MOFs should have suitable pore size and specific functionality that can discriminate the difference in size and physical properties between the two molecules. While rational design of microporous MOFs with desired high productivity for C_3H_4/C_3H_6 separation is quite difficult, we thus systematically screened a series of porous MOFs with different structures, pore sizes, and pore-surface functionalities for this separation. To our surprise, the material UTSA-200 ($[Cu(azpy)_2(SiF_6)]_n$, azpy = 4,4′-azopyridine),[7b] which we recently realized for the highly efficient C_2H_2/C_2H_4 separation, turned out to be very powerful as well for the more difficult C_3H_4/C_3H_6 separation. Our detailed studies comprehensively affirm its benchmark separation performance with the record C_3H_4 uptake capacity (95 cm^{-3} cm^{-3} at 0.01 bar and 298 K), gas selectivity (over 20000), and C_3H_6 productivity (62.0 and 142.8 mmol g^{-1} for 1:99 and 0.1:99.9 mixtures).

We first selected 20 different MOFs to examine their C_3H_4 and C_3H_6 adsorption properties and then superficially evaluate their separation potential (see the Supporting Information, Table S1 for detailed structural parameters). As shown in the Supporting Information, Figure S1, achieving the looked-for efficient separation is indeed very challenging for C_3H_4/C_3H_6 separation, and the examined MOFs almost show unsatisfactory separation properties. Despite the daunting challenge, some reported MOFs with strong binding sites toward C_3H_4 (SIFSIX-1-Cu, SIFSIX-2-Cu-i, SIFSIX-3-Ni, and ELM-12) exhibit steep adsorption of C_3H_4 at the low-pressure region over C_3H_6, leading to the benchmark selectivity reported so far. However, their pore sizes allow the passage of both C_3H_4 and C_3H_6, thus delimiting their high gas selectivities.[9] UTSA-200, with a smaller aperture size of 3.4 Å, exhibits an exceptionally high C_3H_4 uptake but very little C_3H_6 adsorption at the low-pressure region (Figure 1), offering the potential to be the best candidate for C_3H_4/C_3H_6 separation.

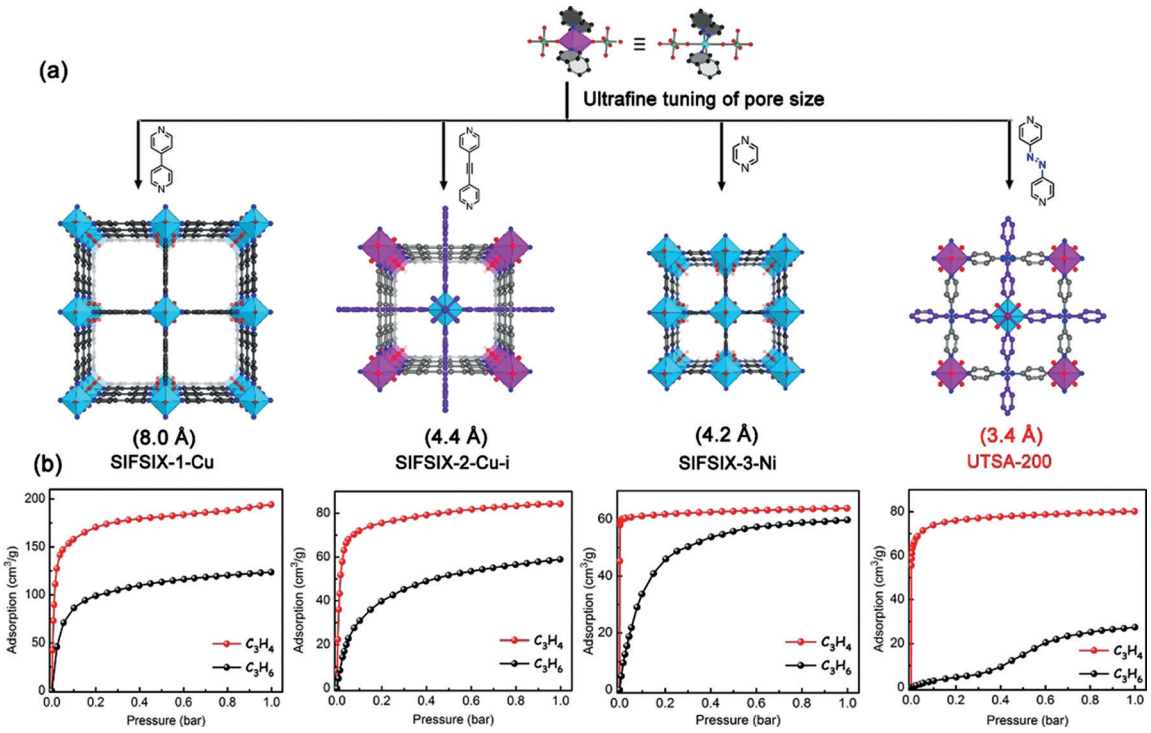

Figure 1. a) The pore aperture and pore chemistry of SIFSIX materials. b) Associated C_3H_4 and C_3H_6 adsorption isotherms at 298 K.

Structural analysis revealed that pore sizes in SIFSIX-1-Cu, SIFSIX-2-Cu-i, and SIFSIX-3-Ni range from microporous (8.0 Å) to ultra-microporous (4.2 Å, Figure 1a),[7a,10] indeed allowing both C_3H_4 and C_3H_6 to enter the pores. The doubly interpenetrated UTSA-200 possesses much smaller channels of 3.4 Å.[7b] This static pore size is notably less than both of C_3H_4 and C_3H_6, which might induce the selective sieving toward the larger C_3H_6 molecules when the framework flexibility and thus slightly enlarged pore sizes are taken into the account. Furthermore, there exist a large number of SiF_6^{2-} anions around the channels that show much stronger binding affinity toward alkynes over alkenes.[7a,9b] These structural features on UTSA-200 might be responsible for the exceptional performance for C_3H_4/C_3H_6 separation. Bulk purity of UTSA-200 sample was confirmed by powder X-ray diffraction (PXRD) patterns and the measured surface area (Supporting Information, Figure S2).[11]

All of these SIFSIX materials show steep and high C_3H_4 uptakes over C_3H_6 at 298 K (Figure 1b). When the pore size was gradually reduced from SIFSIX-1-Cu to UTSA-200, the C_3H_4 sorption isotherms at low-pressure region (0–0.01 bar) become steeper and steeper (Figure 2a). The C_3H_4 capture capacity at 0.01 bar increases in the order of SIFSIX-1-Cu < SIFSIX-2-Cu-I < SIFSIX-3-Ni < UTSA-200 (Figure 2b), wherein UTSA-200 shows the highest value of 95 $cm^3 cm^{-3}$. Even under an ultralow C_3H_4 partial pressure (1000 ppm), the C_3H_4 uptake capacity of UTSA-200 can reach 83 $cm^3 cm^{-3}$, still notably higher than SIFSIX-3-Ni (75 $cm^3 cm^{-3}$), SIFSIX-2-Cu-i (11 $cm^3 cm^{-3}$), and ZU-62 (5.2 $cm^3 cm^{-3}$). In comparison to other top-performing materials, UTSA-200 also sets new benchmarks at both 0.01 and 0.001 bar (Figure 2c; Supporting Information, Figure S3), making it the most promising material for the trace C_3H_4 removal. In contrast, UTSA-200 shows an ignorable C_3H_6 uptake at 0.01 bar (Figure 2b), and little C_3H_6 uptake up to 0.4 bar (10.5 $cm^3 cm^{-3}$), which is dramatically lower than SIFSIX-2-Cu-i (61.2 $cm^3 cm^{-3}$), SIFSIX-3-Ni (85.1 $cm^3 cm^{-3}$) and ZU-62 (69.7 $cm^3 cm^{-3}$) at 0.4 bar. The fine-tuned pore size of UTSA-200 indeed supports the molecular exclusion of C_3H_6 at low pressures. Most importantly, the sieving effect of C_3H_6 can be strengthened with the temperature increased to 318 K while the low-pressure C_3H_4 uptake capacity can be retained (Supporting Information, Figure S5), indicating its bright promise for C_3H_4/C_3H_6 separation at a broader operation temperature.

Ideal adsorbed solution theory (IAST) was utilized to calculate the adsorption selectivity of these materials for a 1:99 (v/v) C_3H_4/C_3H_6 mixture at 298 K. UTSA-200 exhibits an extraordinary high selectivity of over 20000 (Figure 2d; Supporting Information, Figure S7), significantly higher than the previous benchmark ELM-12 (83), SIFSIX-3-Ni (76), and ZU-62 (48). It should be noted that the selectivity of UTSA-200 can be only used for the qualitative comparison. As shown in the Supporting Information, Figure S8, the uptake ratio of C_3H_4/C_3H_6 for UTSA-200 at 0.01:0.01 and 0.01:0.99 bar can reach 149.5 and 2.49, respectively. Both values are the highest among the indicated MOFs, further confirming its best C_3H_4/C_3H_6 selectivity. Furthermore, UTSA-200 also exhibits the record C_3H_4 uptake (2.88 mmol g^{-1}) for adsorption from this mixture (Figure 2e).

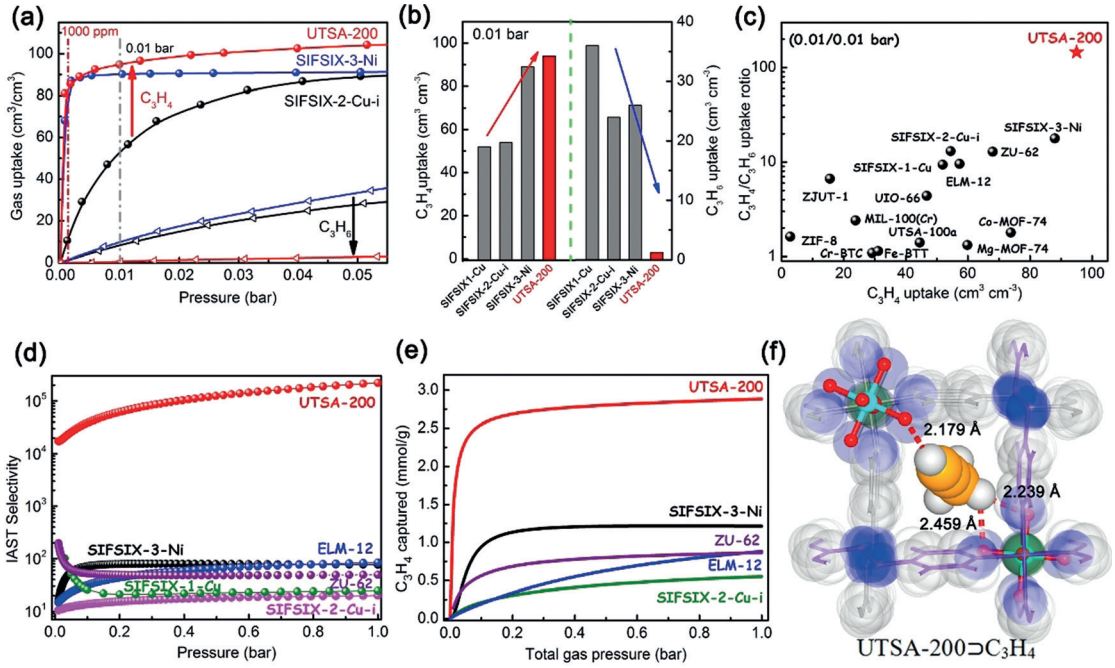

Figure 2. a) Experimental C_3H_4 and C_3H_6 adsorption isotherms of SIFSIX-2-Cu-i (black), SIFSIX-3-Ni (blue), and UTSA-200 (red) at 298 K in the region of 0–0.05 bar. b) Comparison of C_3H_4 and C_3H_6 uptake at 0.01 bar for the SIFSIX materials. c) A comparison of C_3H_4/C_3H_6 uptake ratio at 0.01:0.01 bar for UTSA-200 and other indicated MOFs. d) IAST selectivity and e) IAST calculated C_3H_4 uptake capacity of the indicated MOFs from 1:99 (v/v) gas mixtures. f) DFT-D calculated structure and binding site of UTSA-200⊃C_3H_4. The different nets are highlighted in purple and gray for clarity. Cu cyan, Si dark green, F red, N blue, C gray, H white, C in C_3H_4 orange.

To understand the origin of the ultra strong C_3H_4 adsorption and effective C_3H_6 sieving, we performed detailed modeling studies using first-principles dispersion-corrected density functional theory (DFT-D) method on UTSA-200. The static pore size of UTSA-200, based on the crystal structure, is about 3.4 Å,[7b] which is much smaller than both C_3H_4 (4.2 Å) and C_3H_6 (4.6 Å).[2a] As shown in the Supporting Information, Figure S9, after adsorption of C_3H_4 molecules, the N=N bond and pyridine rings on the azpy exhibit an obvious rotation and distortion, which enlarges the pore to about 4.2 Å, thereby allowing the passing of a C_3H_4 molecule. Calculations also show that each adsorbed C_3H_4 molecule is bound by two SiF_6^{2-} sites from different nets through cooperative C–H···F and C≡H···F H-bonding, with the short distance of 2.179 and 2.239/2.459 Å (Figure 2 f). Owing to the larger size of C_3H_6, the pore needs to be expanded more for the passage (Supporting Information, Figure S10). The calculated static binding energies for C_3H_4 and C_3H_6 are 62.3 kJ mol^{-1} and 45.4 kJ mol^{-1}, respectively. The framework thus has much stronger binding with C_3H_4 molecule than C_3H_6, as further confirmed by the higher experimental isosteric heat of adsorption (Q_{st}) for C_3H_4 (Supporting Information, Figure S11). This kind of subtle guest-assisted pore opening is primarily dictated by the interaction strength of the adsorbate framework: the stronger the intermolecular interactions are, the lower the gate-opening pressure will be.[6b,12] Therefore, attributed to the smaller size and the stronger interactions with the framework, C_3H_4 molecule might open the pore easily to result in the ultrastrong C_3H_4 adsorption. Conversely, the larger size and weaker interactions of C_3H_6 molecule make the pore opening more difficult and thereby to be size-excluded, especially at the low-pressure region.

High-resolution neutron powder diffraction (NPD) measurements were further performed on a C_3D_4-loaded sample of UTSA-200 at 298 K to confirm the calculated C_3H_4 binding sites. The data indicate that C_3D_4 adsorption indeed induced a lot of local framework distortion in the sample (to accommodate the large gas molecules), resulting in lower overall crystal symmetry. Consequently, it became impractical to perform a rigorous Rietveld refinement of the NPD data. Fortunately, it is still possible to qualitatively compare the experimental data with the simulated NPD pattern based on a model structure built upon the DFT-D calculation results. As shown in the Supporting Information, Figure S12, the two agree reasonably well, and thus strongly support the validity of the DFT-D determined C_3H_4 binding configuration.

Transient breakthrough simulations were first conducted for UTSA-200 and the indicated MOFs in fixed-bed adsorption processes to determine the feasibility of C_3H_4/C_3H_6 separation. The 1:99 (v/v) C_3H_4/C_3H_6 mixture was employed as feeds to mimic the industrial process conditions. As depicted in Figure 3 a, efficient separations were realized with all the examined MOFs, whereby C_3H_6 first eluted through the bed to yield a polymer-grade gas, and then C_3H_4 broke through from the bed at a certain time τ_{break}. Owing to the record selectivity and C_3H_4 uptake capacity, UTSA-200 exhibits the longest τ_{break} value, several times higher than that in SIFSIX-3-Ni, ELM-12, and ZU-62 (Supporting Information, Figure S13). During the time 0–τ_{break}, the pure C_3H_6

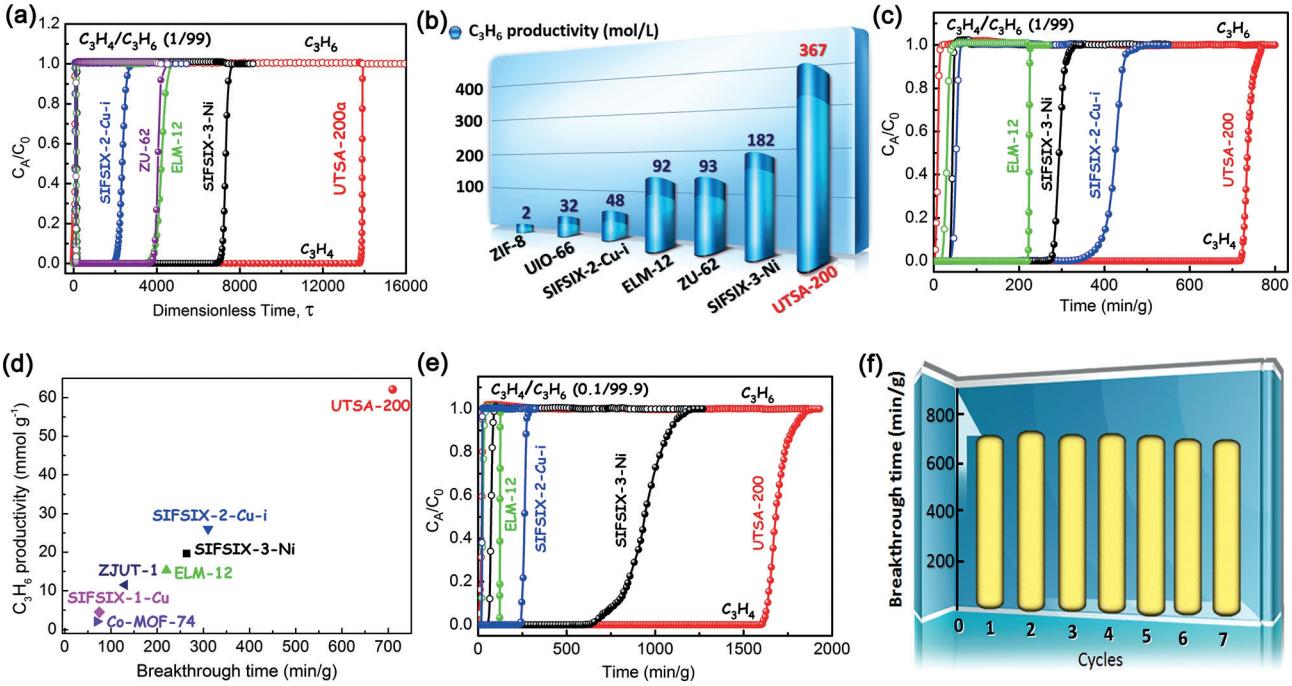

Figure 3. a) Transient breakthrough simulations of C_3H_4/C_3H_6 (1:99, v/v) mixture on UTSA-200 versus some benchmark materials at 298 K. b) Plots of the productivity of pure C_3H_6 from C_3H_4/C_3H_6 mixtures in the simulated breakthrough for the indicated MOFs. c) Experimental breakthrough curves for 1:99 (v/v) mixture under a flow of 2.0 mL min^{-1} at 298 K and 1.01 bar. d) The C_3H_6 productivity from C_3H_4/C_3H_6 mixtures of the indicated MOFs, with C_3H_4 concentration less than 1 ppm. e) Experimental breakthrough curves for a 0.1:99.9 (v/v) mixture. f) Retained time of C_3H_6 in cycling tests of UTSA-200 for a 1:99 (v/v) mixture.

productivity by UTSA-200 can reach 367.2 mol L^{-1} (Figure 3b), which is notably higher than that of SIFSIX-3-Ni, ZU-62, and ELM-12.

Experimental breakthrough studies were performed in a packed column of activated UTSA-200 under flow (2.0 mL min^{-1}) of binary C_3H_4/C_3H_6 (1:99, v/v) mixtures at 298 K, and compared with the indicated MOFs. The breakthrough data depicted in Figure 3c clearly demonstrate that UTSA-200 can effectively separate C_3H_4/C_3H_6 mixtures: the C_3H_6 gas passed through the adsorption bed immediately, while C_3H_4 was retained in the packed column over 710 min g^{-1}. This breakthrough time of C_3H_4 is three times longer than that of SIFSIX-2-Cu-i, ELM-12, and SIFSIX-3-Ni. These experimental data are consistent well with the simulated results. The concentration of C_3H_4 in the outlet effluent was even below 1 ppm up to 700 min (Supporting Information, Figure S14), which is notably less than the acceptable level of less than 5 ppm for polymer-grade C_3H_6 gas. It is to be noted that this deep removal of C_3H_4 from 1:99 (v/v) mixture is unable to be achieved for most selected MOFs (such as MOF-74 series, Cu-BTC, ZIF-8, MIL-100) owing to their unsatisfied selectivity (Supporting Information, Figure S15). Among the viable MOFs, the C_3H_6 production of UTSA-200 from the outlet effluent for a given cycle was calculated to be record high of 62.9 mmol g^{-1} (Figure 3d; Supporting Information, Table S14), far exceeding those observed in SIFSIX-3-Ni (19.6 mmol g^{-1}) and ELM-12 (15.8 mmol g^{-1}). For C_3H_4/C_3H_6 mixture containing ultralow C_3H_4 concentration (1000 ppm), UTSA-200 also exhibits the best separation performance with the record C_3H_6 production of 143.8 mmol g^{-1}, as illustrated in Figure 3e and the Supporting Information, Table S15. Finally, the separation performance of UTSA-200 can be recycled at least 7 times (Figure 3f; Supporting Information, Figures S17–S22).

Through a comprehensive screening of broad types of MOFs, we demonstrated herein an ultra-microporous MOF, UTSA-200, as the best separating material for the removal of trace C_3H_4 from C_3H_4/C_3H_6 mixtures. The foregoing results revealed that UTSA-200 exhibits both the unprecedented high C_3H_4 capture capacity and separation selectivity, setting new benchmarks for any material reported so far. This exceptional separation performance is attributed to the framework flexibility originated from the rotation of pyridine rings inside the pores and the strong binding sites that can selectively block the larger C_3H_6 but capture large amount of the preferred smaller C_3H_4 at low-pressure region. Breakthrough experiments confirmed that UTSA-200 can completely remove trace C_3H_4 from 1:99 and 0.1:99.9 (v/v) mixtures, affording the record-high C_3H_6 production scale with 99.9999% purity. This work not only reports the best porous material for C_3H_4/C_3H_6 separation, but also demonstrates that framework flexibility can be utilized to target some very challenging gas separations, thus fully fulfilling the promise of emerging microporous MOFs for gas separations in the future.

Acknowledgements

This research was supported by the National Natural Science Foundation of China (21606163, 21576006) and the Welch Foundation (grant AX-1730).

Conflict of interest

The authors declare no conflict of interest.

Keywords: gas separation · porous materials · propylene purification · propyne · size sieving

How to cite: *Angew. Chem. Int. Ed.* **2018**, *57*, 15183–15188
Angew. Chem. **2018**, *130*, 15403–15408

[1] a) D. S. Sholl, R. P. Lively, *Nature* **2016**, *532*, 435–437; b) S. Chu, Y. Cui, N. Liu, *Nat. Mater.* **2017**, *16*, 16–22; c) J. Y. S. Lin, *Science* **2016**, *353*, 121–122.

[2] a) J. R. Li, R. J. Kuppler, H. C. Zhou, *Chem. Soc. Rev.* **2009**, *38*, 1477–1504; b) H. Furukawa, K. E. Cordova, M. O'Keeffe, O. M. Yaghi, *Science* **2013**, *341*, 974–986; c) P. Li, N. A. Vermeulen, C. D. Malliakas, D. A. Gómez-Gualdrón, A. J. Howarth, B. L. Mehdi, A. Dohnalkova, N. D. Browning, M. O'Keeffe, O. K. Farha, *Science* **2017**, *356*, 624–627; d) B. Li, M. Chrzanowski, Y. Zhang, S. Ma, *Coord. Chem. Rev.* **2016**, *307*, 106–129.

[3] a) J.-R. Li, J. Sculley, H.-C. Zhou, *Chem. Rev.* **2012**, *112*, 869–932; b) X. Zhao, Y. Wang, D. S. Li, X. Bu, P. Feng, *Adv. Mater.* **2018**, *30*, 1705189; c) H. Sato, W. Kosaka, R. Matsuda, A. Hori, Y. Hijikata, R. V. Belosludov, S. Sakaki, M. Takata, S. Kitagawa, *Science* **2014**, *343*, 167–170; d) P.-Q. Liao, N.-Y. Huang, W.-X. Zhang, J.-P. Zhang, X.-M. Chen, *Science* **2017**, *356*, 1193–1196; e) H. Wang, X. Dong, J. Lin, S. J. Teat, S. Jensen, J. Cure, E. V. Alexandrov, Q. Xia, K. Tan, Q. Wang, D. H. Olson, D. M. Proserpio, Y. J. Chabal, T. Thonhauser, J. Sun, Y. Han, J. Li, *Nat. Commun.* **2018**, *9*, 1745; f) X. Han, H. G. W. Godfrey, L. Briggs, A. J. Davies, Y. Cheng, L. L. Daemen, A. M. Sheveleva, F. Tuna, E. J. L. McInnes, J. Sun, C. Drathen, M. W. George, A. J. Ramirez-Cuesta, K. M. Thomas, S. Yang, M. Schröder, *Nat. Mater.* **2018**, *17*, 691–696; g) J. W. Yoon, H. Chang, S.-J. Lee, Y. K. Hwang, D.-Y. Hong, S.-K. Lee, J. S. Lee, S. Jiang, T.-U. Yoon, K. Kwac, Y. Jung, R. S. Pillai, F. Faucher, A. Vimont, M. Daturi, G. Férey, C. Serre, G. Maurin, Y.-S. Bae, J.-S. Chang, *Nat. Mater.* **2017**, *16*, 526–531; h) D. A. Reed, B. K. Keitz, J. Oktawiec, J. A. Mason, T. Runčevski, D. J. Xiao, L. E. Darago, V. Crocellà, S. Bordiga, J. R. Long, *Nature* **2017**, *550*, 96–100; i) H.-M. Wen, L. Li, R.-B. Lin, B. Li, B. Hu, W. Zhou, J. Hu, B. Chen, *J. Mater. Chem. A* **2018**, *6*, 6931–6937; j) Y.-S. Bae, C. Y. Lee, K. C. Kim, O. K. Farha, P. Nickias, J. T. Hupp, S. T. Nguyen, R. Q. Snurr, *Angew. Chem. Int. Ed.* **2012**, *51*, 1857–1860; *Angew. Chem.* **2012**, *124*, 1893–1896.

[4] K. Sumida, D. L. Rogow, J. A. Mason, T. M. McDonald, E. D. Bloch, Z. R. Herm, T.-H. Bae, J. R. Long, *Chem. Rev.* **2012**, *112*, 724–781.

[5] K. Adil, Y. Belmabkhout, R. S. Pillai, A. Cadiau, P. M. Bhatt, A. H. Assen, G. Maurin, M. Eddaoudi, *Chem. Soc. Rev.* **2017**, *46*, 3402–3430.

[6] a) P. Nugent, Y. Belmabkhout, S. D. Burd, A. J. Cairns, R. Luebke, K. Forrest, T. Pham, S. Ma, B. Space, L. Wojtas, M. Eddaoudi, M. J. Zaworotko, *Nature* **2013**, *495*, 80–84; b) A. Cadiau, K. Adil, P. M. Bhatt, Y. Belmabkhout, M. Eddaoudi, *Science* **2016**, *353*, 137–140; c) H. Wang, X. Dong, E. Velasco, D. H. Olson, Y. Han, J. Li, *Energy Environ. Sci.* **2018**, *11*, 1226–1231.

[7] a) X. Cui, K. Chen, H. Xing, Q. Yang, R. Krishna, Z. Bao, H. Wu, W. Zhou, X. Dong, Y. Han, B. Li, Q. Ren, M. J. Zaworotko, B. Chen, *Science* **2016**, *353*, 141 – 144; b) B. Li, X. Cui, D. O'Nolan, H.-M. Wen, M. Jiang, R. Krishna, H. Wu, R.-B. Lin, Y. S. Chen, D. Yuan, H. Xing, W. Zhou, Q. Ren, G. Qian, M. J. Zaworotko, B. Chen, *Adv. Mater.* **2017**, *29*, 1704210; c) R.-B. Lin, L. Li, H. Wu, H. Arman, B. Li, R.-G. Lin, W. Zhou, B. Chen, *J. Am. Chem. Soc.* **2017**, *139*, 8022 – 8028; d) J. Lee, C. Y. Chuah, J. Kim, Y. Kim, N. Ko, Y. Seo, K. Kim, T. H. Bae, E. Lee, *Angew. Chem. Int. Ed.* **2018**, *57*, 7869 – 7873; *Angew. Chem.* **2018**, *130*, 7995 – 7999.

[8] C. R. Reid, K. M. Thomas, *J. Phys. Chem. B* **2001**, *105*, 10619 – 10629.

[9] a) L. Li, R.-B. Lin, R. Krishna, X. Wang, B. Li, H. Wu, J. Li, W. Zhou, B. Chen, *J. Am. Chem. Soc.* **2017**, *139*, 7733 – 7736; b) L. Yang, X. Cui, Q. Yang, S. Qian, H. Wu, Z. Bao, Z. Zhang, Q. Ren, W. Zhou, B. Chen, H. Xing, *Adv. Mater.* **2018**, *30*, 1705374; c) L. Yang, X. Cui, Z. Zhang, Q. Yang, Z. Bao, Q. Ren, H. Xing, *Angew. Chem. Int. Ed.* **2018**, *57*, 13145 – 13149; *Angew. Chem.* **2018**, *130*, 13329-13333.

[10] O. Shekhah, Y. Belmabkhout, K. Adil, P. M. Bhatt, A. J. Cairns, M. Eddaoudi, *Chem. Commun.* **2015**, *51*, 13595 – 13598.

[11] a) D. O'Nolan, A. Kumar, M. J. Zaworotko, *J. Am. Chem. Soc.* **2017**, *139*, 8508 – 8513; b) D. O'Nolan, D. G. Madden, A. Kumar, K.-J. Chen, T. Pham, K. A. Forrest, E. Patyk-Kazmierczak, Q.-Y. Yang, C. A. Murray, C. C. Tang, B. Space, M. J. Zaworotko, *Chem. Commun.* **2018**, *54*, 3488 – 3491.

[12] a) C. Gücüyener, J. van den Bergh, J. Gascon, F. Kapteijn, *J. Am. Chem. Soc.* **2010**, *132*, 17704 – 17706; b) N. Nijem, H. Wu, P. Canepa, A. Marti, K. J. Balkus, Jr., T. Thonhauser, J. Li, Y. J. Chabal, *J. Am. Chem. Soc.* **2012**, *134*, 15201 – 15204.

Manuscript received: September 1, 2018
Accepted manuscript online: September 21, 2018
Version of record online: October 15, 2018

Angewandte Chemie
Eine Zeitschrift der Gesellschaft Deutscher Chemiker

Supporting Information

A Metal–Organic Framework with Suitable Pore Size and Specific Functional Sites for the Removal of Trace Propyne from Propylene

Libo Li, Hui-Min Wen, Chaohui He, Rui-Biao Lin, Rajamani Krishna, Hui Wu, Wei Zhou, Jinping Li, Bin Li, and Banglin Chen**

anie_201809869_sm_miscellaneous_information.pdf

SUPPORTING INFORMATION

Table of Contents

Experimental Procedures

General Materials and MOF Synthesis

The selected SIFSIX materials (SIFSIX-1-Cu, SIFSIX-2-Cu-i, SIFSIX-3-Ni, and UTSA-200) were synthesized using methods reported in the corresponding literatures.[1-4] The phase purity of the bulk materials was confirmed by PXRD (Figure S2). Powder X–ray diffraction (PXRD) patterns were measured by a BRUKER D8 ADVANCE diffractometer employing Cu-K_α radiation operated at 30 kV and 15 mA, scanning over the range 5-40° (2θ) at a rate of 1°/min. **Note that the synthesis of UTSA-200 needs careful control of the reaction condition; because a small amount of impurities are easily produced during the production of UTSA-200,[5,6] which would greatly affect the separation performance**. In this work, the bulk purity of UTSA-200 was undoubtedly confirmed by PXRD patterns and the measured surface area/pore volume (617 $m^2\ g^{-1}$ and 0.27 $cm^3\ g^{-1}$, Figure S2), which is consistent well with the theoretical ones calculated from the crystal structure (597 $m^2\ g^{-1}$ and 0.26 $cm^3\ g^{-1}$). C_3H_4 (99.99%), C_3H_6 (99.99%), He (99.999%) and mixed gases of C_3H_4/C_3H_6 = 1/99 (v/v), C_3H_4/C_3H_6 = 0.1/99.9 (v/v) were purchased from Beijing Special Gas Co. LTD (China). All starting chemicals and solvents were purchased from commercial companies and used without further purification.

Gas sorption measurements

An Intelligent Gravimetric Analyzer (IGA 001, Hiden, UK) was used to measure gas adsorption isotherms. ThermoFisher water bath is used to keep the adsorption tube at a constant temperature of 273, 298, 308, and 318 K. The samples were activated to remove all the guest solvents according to the reported literatures.[34,35]

Breakthrough experiments

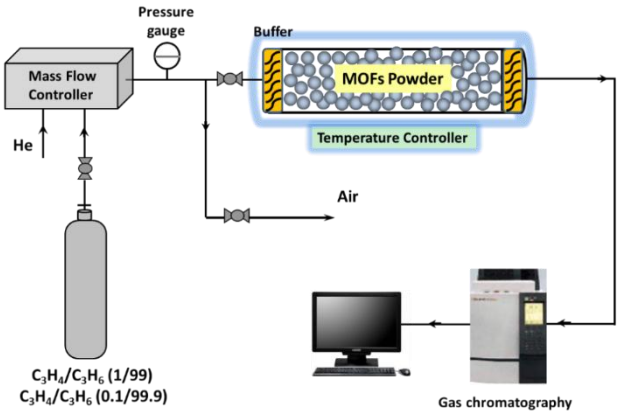

The breakthrough experiments for C_3H_4/C_3H_6 (1/99 and 0.1/99.9) mixtures were carried out at a flow rate of 2 mL/min (298 K, 1.01 bar). Activated MOF powder was packed into Φ 4 × 150 mm stainless steel column under pure N_2 atmosphere (Table S13). The sample in each column was compressed as much as possible to obtain the best separation performance, and column voidages are similar for different samples. The experimental set-up consisted of two fixed-bed stainless steel reactors. One reactor was loaded with the adsorbent, while the other reactor was used as a blank control group to stabilize the gas flow. The horizontal reactors were placed in a temperature controlled environment, maintained at 298 K. The flow rates of all gases mixtures were regulated by mass flow controllers, and the effluent gas stream from the column is monitored by a gas chromatography. Prior to the breakthrough experiment, we activated the sample by flushing the adsorption bed with helium gas for 2 h at 323 K. The adsorption bed was regenerated by He flow (100 mL/min) for 1 h at 298 K.

SUPPORTING INFORMATION

Neutron diffraction experiment

Powder neutron diffraction data were collected using the BT-1 neutron powder diffractometer at the National Institute of Standards and Technology (NIST) Center for Neutron Research. A Ge(311) monochromator with a 75° take-off angle, λ = 2.0787(2) Å, and in-pile collimation of 60 minutes of *arc* was used. Data were collected over the range of 1.3-166.3° (2θ) with a step size of 0.05°. Fully activated UTSA-200 sample was loaded in a vanadium can equipped with a capillary gas line. A closed-cycle He refrigerator was used to control the sample temperature. The bare MOF sample was measured first at the temperatures of 298 K. To probe the C_3H_4 adsorption locations, a pre-determined pressure (1 bar) of C_3D_4 were loaded into the sample at room temperature. Diffraction data were then collected on the C_3D_4-loaded UTSA-200 samples. (Note: deuterated gas C_3D_4 was used to avoid the large incoherent neutron scattering background that would be produced by the hydrogen in C_3H_4.

Fitting of pure component isotherms

To calculate the C_3H_4/C_3H_6 adsorption selectivity for UTSA-200, SIFSIX-3-Ni, SIFSIX-2-Cu-i, and ELM-12 at 298 K, pure component isotherms of these four MOFs were fitted with Dual-site Langmuir-Freundlich model.

$$q = q_{A,sat}\frac{b_A p^{\nu A}}{1+b_A p^{\nu A}} + q_{B,sat}\frac{b_B p^{\nu B}}{1+b_B p^{\nu B}} \quad (1)$$

with T-dependent parameters b_A, and b_B

$$b_A = b_{A0}\exp\left(\frac{E_A}{RT}\right); \quad b_B = b_{B0}\exp\left(\frac{E_B}{RT}\right) \quad (2)$$

The fitting parameters for C_3H_4 and C_3H_6 are provided in Table S3-S11. Figure S6 presents a comparison of experimental data for adsorption isotherms C_3H_4 and C_3H_6 in UTSA-200, SIFSIX-3-Ni, SIFSIX-2-Cu-i, and ELM-12 with dual-site Langmuir model fits. The fits are of good accuracy for both guest molecules.

In order to compare the C_3H_4/C_3H_6 separation potential of various MOFs, IAST calculations of mixture adsorption were performed. For separation of a binary mixture of components A and B, the adsorption selectivity is defined by

$$S_{ads} = \frac{q_A/q_B}{y_A/y_B} \quad (3)$$

where the q_A, and q_B represent the molar loadings within the MOF that is in equilibrium with a bulk fluid mixture with mole fractions y_A, and y_B = 1 - y_A. The molar loadings, also called *gravimetric uptake capacities*, are usually expressed with the units mol kg^{-1}. The IAST calculations of C_3H_4/C_3H_6 adsorption selectivites taking the mole fractions y_A = 0.01 and y_B = 1 - y_A = 0.99 for a total pressure of 100 kPa and 298 K.

The separations in fixed bed absorbers are also influenced by the uptake capacities. The *volumetric uptake capacities* are

$$Q_A = \rho q_A; \quad Q_B = \rho q_B \quad (4)$$

where is the crystal framework density of the MOF, expressed say in units of kg m^{-3}, or kg L^{-1}. The objective of C_3H_4/C_3H_6 separations is to obtain pure C_3H_6. Krishna has defined a combined selectivity/capacity metric, called the *separation potential*[7]

$$\Delta Q = Q_A\frac{y_B}{1-y_B} - Q_B \quad (5)$$

The physical significance of ΔQ, conveniently expressed in the units of mol per L of adsorbent, is that it represents the *maximum* amount of pure component B (less strongly adsorbed component) that can be recovered during the *adsorption* phase of fixed bed separations. The quantity *Q* is an appropriate combination of selectivity and uptake capacity that is reflective of the separations in fixed beds packed with a specific adsorbent.

Isosteric heat of adsorption

The binding energies of C_3H_4 and C_3H_6 in the MOFs are reflected in the isosteric heat of adsorption, Q_{st}, defined as

$$Q_{st} = RT^2\left(\frac{\partial \ln p}{\partial T}\right)_q \quad (6)$$

These values were determined using the pure component isotherm fits using the Virial equation (Figure S11). Q_{st} is the coverage-dependent isosteric heat of adsorption and *R* is the universal gas constant. The heat enthalpy of C_3H_4 adsorption for UTSA-200 are determined by the adsorption data measured from 0-1 bar at 298, 308, and 318 K.

Density functional theory (DFT) calculations

First-principles density-functional theory (DFT) calculations were performed using the Quantum-Espresso package.[48] A semi-empirical addition of dispersive forces to conventional DFT was included in the calculation to account for van der Waals interactions.[49] We used Vanderbilt-type ultrasoft pseudopotentials and generalized gradient approximation (GGA) with Perdew-Burke-Ernzerhof (PBE) exchange correlation. A cutoff energy of 544 Ev and a 2×2×4 k-point mesh (generated using the Monkhosrt-Pack scheme) were found to be enough for the total energy to converge within 0.01 meV/atom. We first optimized the structure of UTSA-200. The optimized structures are good matches for the experimentally determined crystal structures of the coordination networks. Various guest gas molecules were then introduced to various locations of the channel pore, followed by a full structural relaxation. To obtain the gas binding energy, an isolated gas molecule placed in a supercell (with the same cell dimensions as the MOF crystal) was also relaxed as a reference. The static binding energy (at T = 0 K) was then calculated using: E_B = E(MOF) + E(gas) – E(MOF+gas).

Transient breakthrough of C_3H_4/C_3H_6 mixtures in fixed bed adsorbers

The performance of industrial fixed bed adsorbers is dictated by a combination of adsorption selectivity and uptake capacity. Transient breakthrough simulations were carried out for 1/99 C_3H_4/C_3H_6 mixtures operating at a total pressure of 100 kPa and 298 K, using the methodology described in earlier publications. For the breakthrough simulations, the following parameter values were used: length of packed bed, L = 0.3 m; voidage of packed bed, ε = 0.4; superficial gas velocity at inlet, u = 0.04 m/s. The transient breakthrough simulation results are presented in terms of a *dimensionless* time, τ, defined by dividing the actual time, t, by the characteristic time, $L\varepsilon u^{-1}$.

We investigated the separation performance of UTSA-200 and the indicated MOFs for the separation of 1/99 C_3H_4/C_3H_6 feed mixtures. The transient breakthrough simulations in Figure 3a show the molar concentrations of C_3H_4/C_3H_6 in the gas phase exiting the adsorber packed with MOF adsorbents as a function of the dimensionless time, τ. In these simulations, the total bulk gas phase is at 298 K and 100 kPa; the partial pressures of C_3H_4, and C_3H_6 in the inlet feed gas mixture are, respectively, p_1 = 1 kPa, p_2 = 99 kPa. Analogous breakthrough simulations were performed for UTSA-200 and the other indicated MOFs. On the basis of the gas phase concentrations, we can calculate the impurity level of C_3H_4 in the gas mixture exiting the fixed bed packed with adsorbents; see Figure S13. At a certain time, τ_{break}, the impurity level will exceed the desired purity level of 5 ppm that corresponds to the purity requirement of the feed to the

polymerization reactor. The adsorption cycle needs to be terminated at that time break and the regeneration process needs to be initiated. From a material balance on the adsorber, the amount of C_3H_4 captured during the time interval 0 -τ_{break} can be determined. Figure 3d presents a plot of the amount of C_3H_4 captured plotted as a function of the time interval τ_{break}. The hierarchy of capture capacities is directly related to the corresponding hierarchy of breakthrough times, τ_{break}. UTSA-200 has a significantly higher capture capacity, by more than a factor two, than other MOFs. In addition, we also determined the volumetric productivity of C_3H_6 containing < 5 ppm C_3H_4 (Figure 3b). These volumetric productivities are presented in Table S12. The productivities are linearly related to the IAST calculations of the separation potential ΔQ. The highest productivity is achieved with UTSA-200. Cu-BTC is unable to produce the product with the desired purity of < 5 ppm C_3H_4.

Notation

b_A	Langmuir-Freundlich constant for species *i* at adsorption site A, $\mathrm{Pa}^{-\nu}$
b_B	Langmuir-Freundlich constant for species *i* at adsorption site B, $\mathrm{Pa}^{-\nu}$
E	energy parameter, J mol^{-1}
p_i	partial pressure of species *i* in mixture, Pa
p_t	total system pressure, Pa
q_i	component molar loading of species *i*, mol kg^{-1}
Q_{st}	isosteric heat of adsorption, J mol^{-1}
t	time, s
T	absolute temperature, K

Greek letters

ν	Freundlich exponent, dimensionless

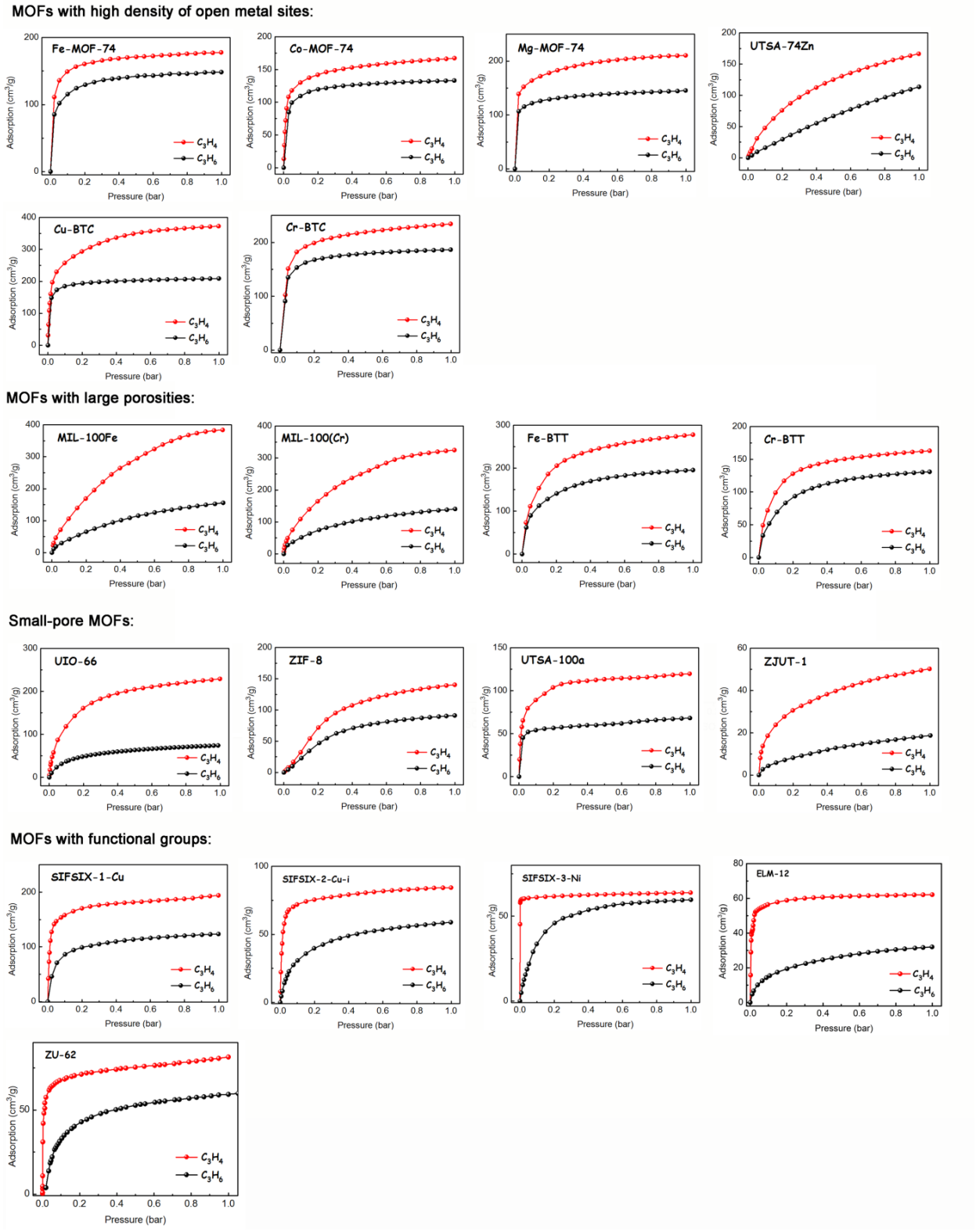

Figure S1. Experimental C_3H_4 (red) and C_3H_6 (black) adsorption isotherms of the selected MOF materials at 298 K, including some MOFs with high density of open metal sites (Fe-MOF-74, Co-MOF-74, Mg-MOF-74, UTSA-74, Cu-BTC, and Cr-BTC), some MOFs with high porosities (MIL-100(Fe), MIL-100(Cr), Fe-BTT, and Cr-BTT), some small-pore MOFs (UIO-66, ZIF-8, UTSA-100, and ZJUT-1), and MOFs with functional SiF_6^{2-} or OTF^- sites (SIFSIX-1-Cu, SIFSIX-2-Cu-i, SIFSIX-3-Ni, ELM-12, and ZU-62). The detailed structural information of these selected MOFs are summarized in Table S1. It was found that achieving the looked-for efficient separation is indeed very challenging for C_3H_4/C_3H_6 separation, and the examined MOFs almost show unsatisfied separation properties. For instance, MOF-74

series render steep and high C_3H_4 adsorption at low pressure, but their selectivity of C_3H_4 over C_3H_6 are quite low because of the equal affinity for both gas molecules toward open metal sites. High porosities in MOFs (such as MIL-100 and Fe-BTT) facilitate high total C_3H_4 uptake amounts at 1 bar, but a slow increase of C_3H_4 adsorption at low pressure and the absence of sieving effect which are detrimental to achieve high selectivity. Further, some ultra-small pore MOFs (3.5–4.0 Å range) without functional sites (such as ZIF-8, UTSA-100) also show unsatisfied adsorption selectivity due to the moderate strong C_3H_4 capture capacity. It is to be noted that those MOFs with strong binding sites toward C_3H_4 (SIFSIX-1-Cu, SIFSIX-2-Cu-i, SIFSIX-3-Ni, ZU-62, and ELM-12) exhibit steep adsorption of C_3H_4 at low-pressure region over C_3H_6, leading to the benchmark selectivity reported so far. However, their pore sizes allow the passage of both C_3H_4 and C_3H_6, thus delimiting their high gas selectivities.

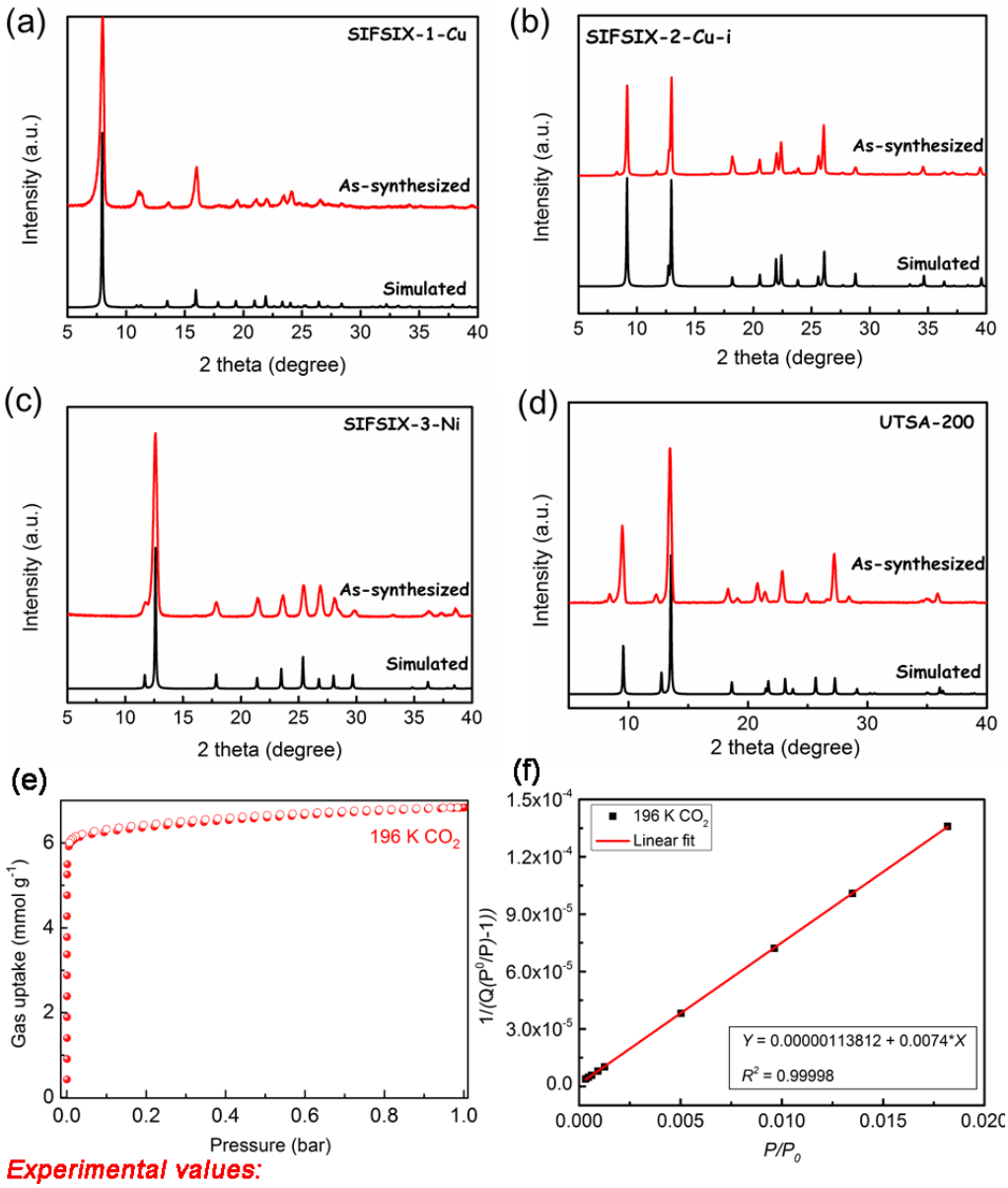

Experimental values:

S_{BET} = (1/(0.0074 -1.13812×10^{-6}))/22414×6.023×10^{23}×0.170×10^{-18} = 617 m^2 g^{-1}

V_p = 0.27 cm^3 g^{-1}

Theoretical values calculated from the crystal structure:

S_{BET} = 597 m^2 g^{-1}; V_p = 0.26 cm^3 g^{-1}

Figure S2. PXRD patterns of as-synthesized sample SIFSIX-1-Cu (a), SIFSIX-2-Cu-i (b), SIFSIX-3-Ni (c), and UTSA-200 (d), along with the simulated XRD pattern from the single-crystal X-ray structure. (e,f) Gas adsorption isotherms of UTSA-200a for CO_2 at 196 K, and the BET surface area and pore volume of UTSA-200 obtained from the 196 K CO_2 isotherms, which is in good agreement with the theoretical values calculated from the crystal structure.

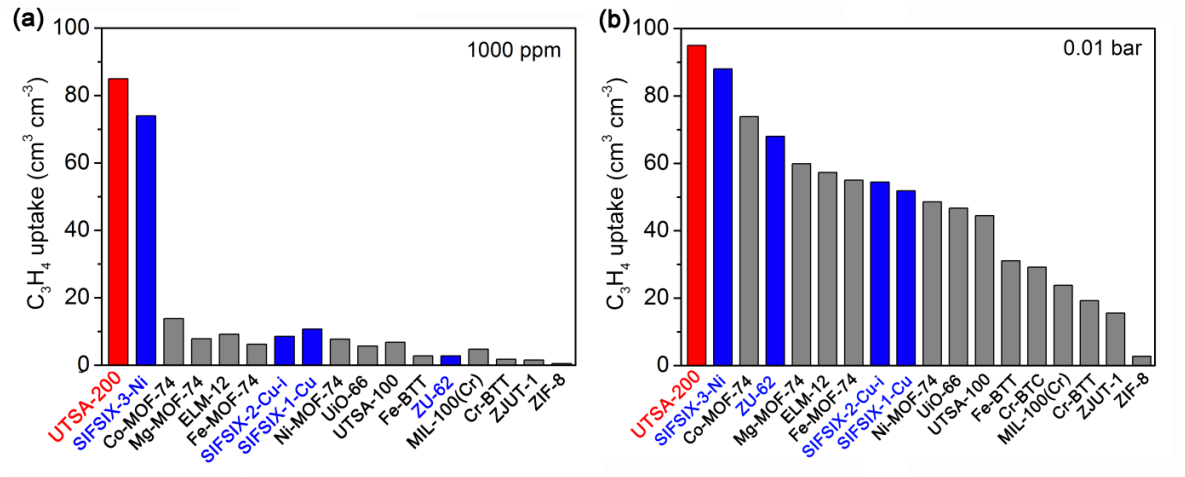

Figure S3. Comparison of C_3H_4 uptake for UTSA-200 and other examined materials at ultralow C_3H_4 partial pressure of 1000 ppm or 0.01 bar and 298 K, indicating that UTSA-200 exhibits the highest C_3H_4 uptake capacity at both 1000 ppm and 0.01 bar.

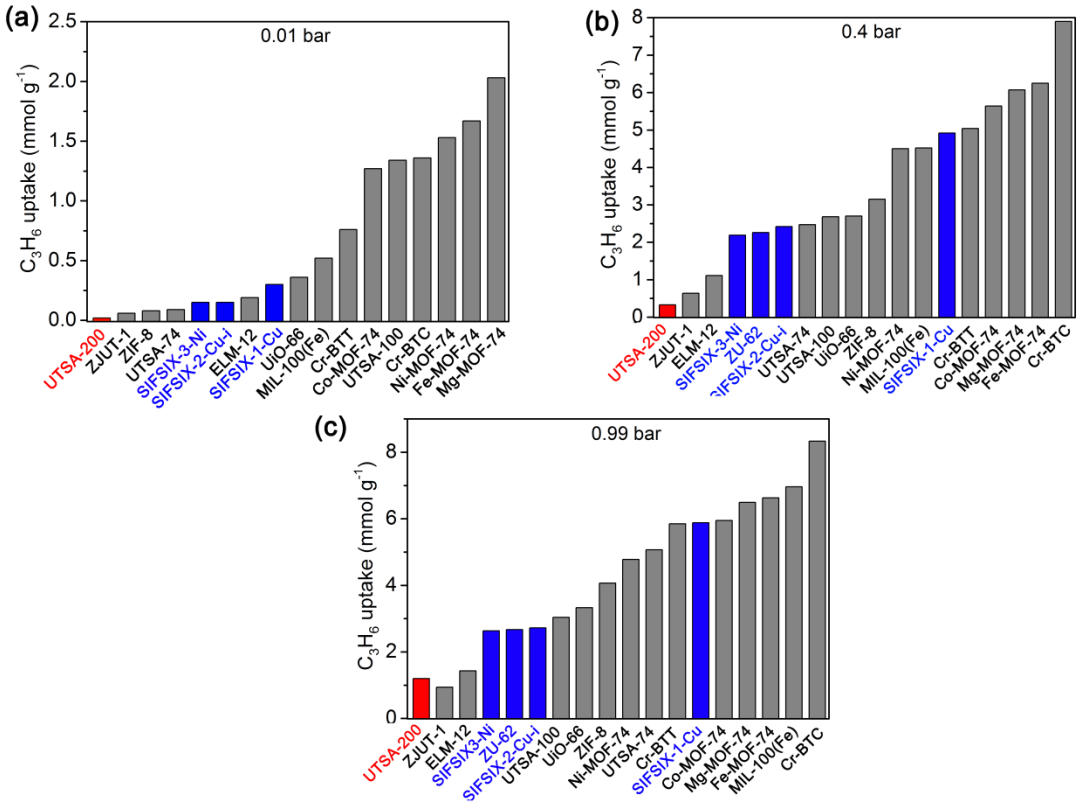

Figure S4. Comparison of C_3H_6 uptake for UTSA-200 and other examined materials at the partial pressure of (a) 0.01 bar; (b) 0.4 bar; (c) 0.99 bar (at 298 K), indicating that UTSA-200 exhibits the lowest C_3H_6 uptake in the entire range of 1.0 bar.

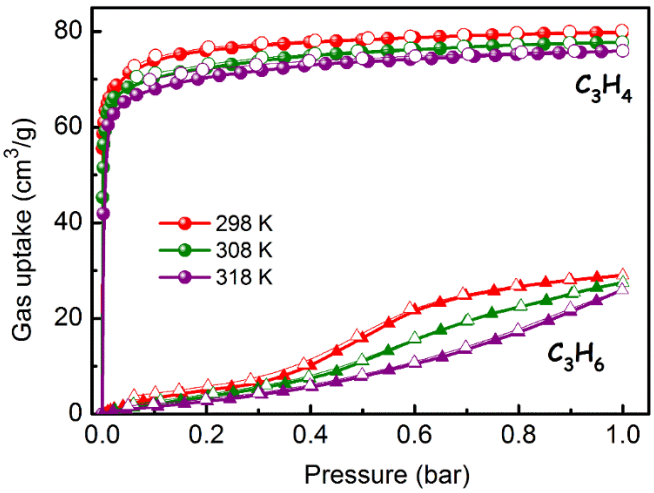

Figure S5. Gas sorption isotherms of C_3H_4 and C_3H_6 for UTSA-200 at 298-318 K. The entrance of C_3H_6 molecule can be efficiently blocked under the pressure lower than 0.4 bar. When the pressure was further increased to 1 bar, C_3H_6 adsorption isotherm slopes up all the time. This is because the N=N bond and the pyridine rings in the MOF linker have certain rotational flexibility, so the pore sizes can be slightly enlarged under higher pressure (larger than 0.4 bar) to take up more C_3H_6 molecules.

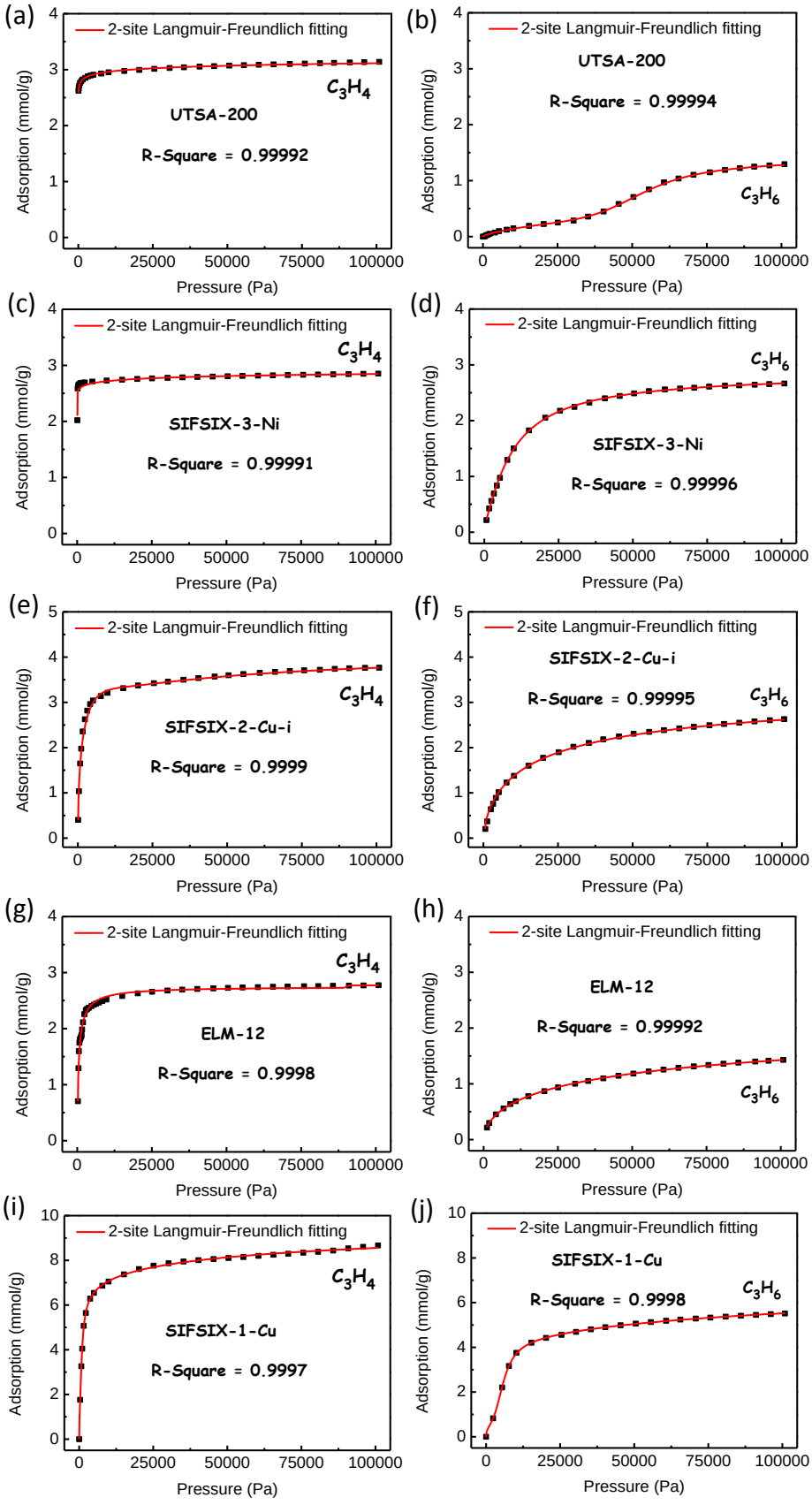
(a)
2-site Langmuir-Freundlich fitting
C_3H_4
UTSA-200
R-Square = 0.99992
(b)
2-site Langmuir-Freundlich fitting
UTSA-200
R-Square = 0.99994
C_3H_6
(c)
2-site Langmuir-Freundlich fitting
C_3H_4
SIFSIX-3-Ni
R-Square = 0.99991
(d)
2-site Langmuir-Freundlich fitting
C_3H_6
SIFSIX-3-Ni
R-Square = 0.99996
(e)
2-site Langmuir-Freundlich fitting
C_3H_4
SIFSIX-2-Cu-i
R-Square = 0.9999
(f)
2-site Langmuir-Freundlich fitting
SIFSIX-2-Cu-i
R-Square = 0.99995
C_3H_6
(g)
2-site Langmuir-Freundlich fitting
C_3H_4
ELM-12
R-Square = 0.9998
(h)
2-site Langmuir-Freundlich fitting
ELM-12
R-Square = 0.99992
C_3H_6
(i)
2-site Langmuir-Freundlich fitting
C_3H_4
SIFSIX-1-Cu
R-Square = 0.9997
(j)
2-site Langmuir-Freundlich fitting
SIFSIX-1-Cu
R-Square = 0.9998
C_3H_6
Adsorption (mmol/g)
Pressure (Pa)
0
25000
50000
75000
100000

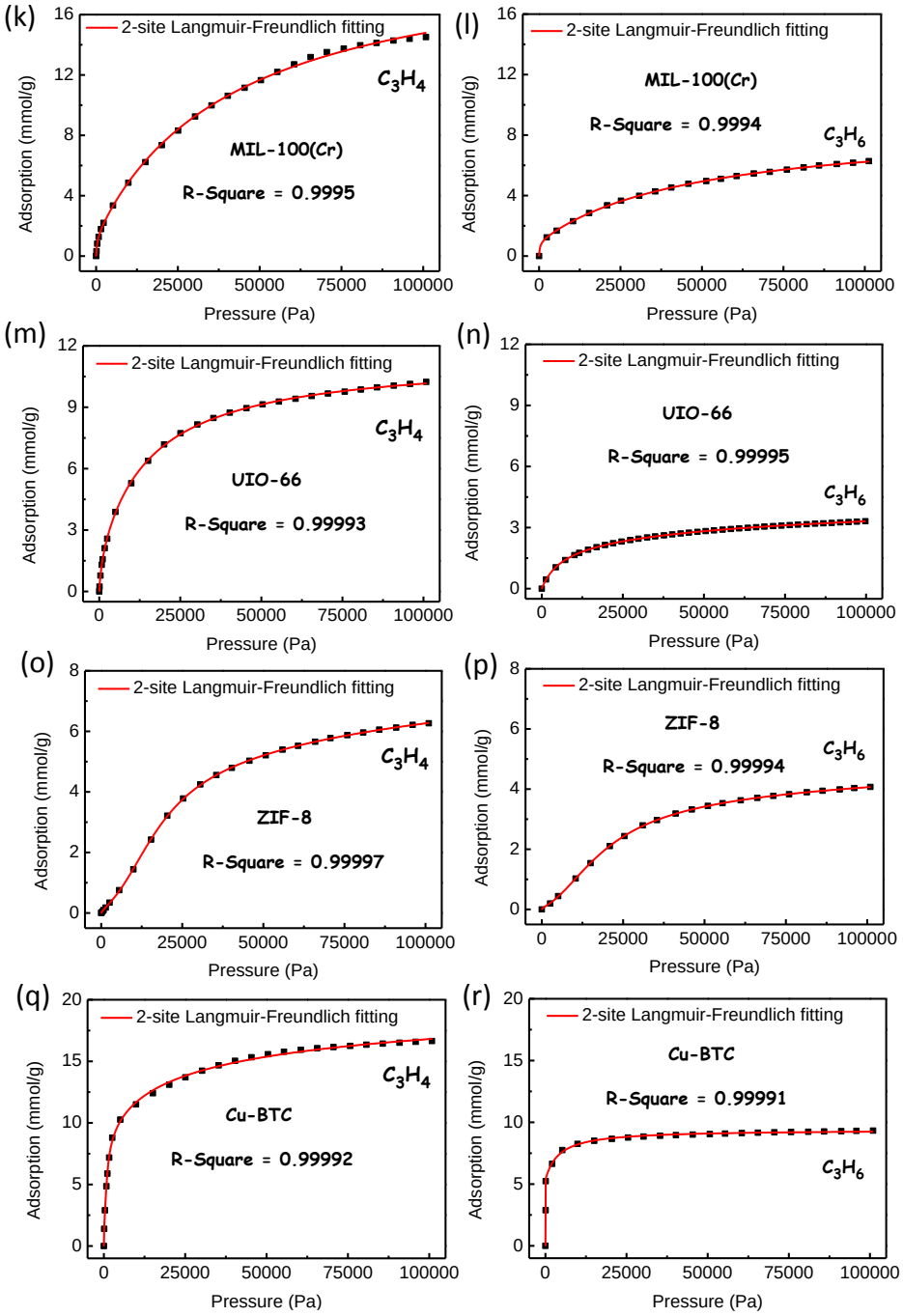

Figure S6. C_3H_4 and C_3H_6 adsorption isotherms at 298 K in selected MOFs with dual-site Langmuir-Freundlich model fits.

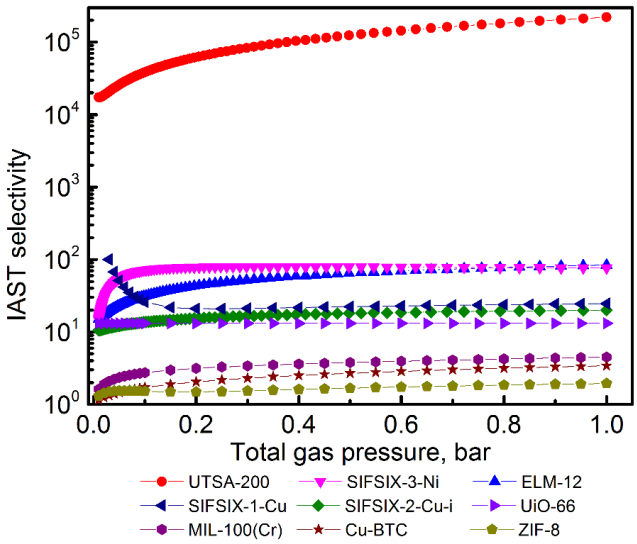

Figure S7. IAST selectivity of UTSA-200 versus the indicated MOF materials.

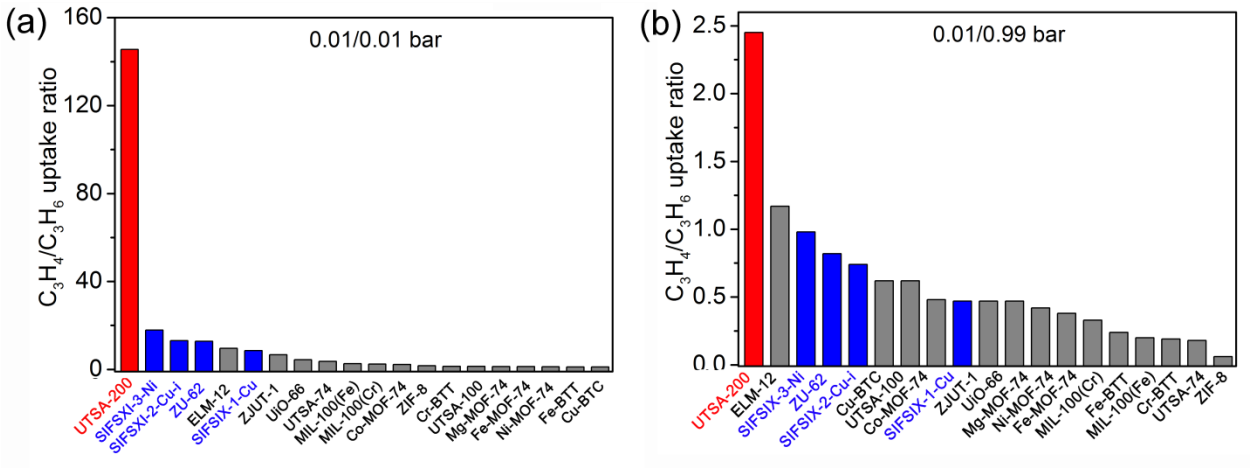

Figure S8. Comparison of C_3H_4/C_3H_6 uptake ratio at 0.01/0.01 bar (a) and 0.01/0.99 bar (b) for UTSA-200 with respect to other top-performing MOF materials as indicated.

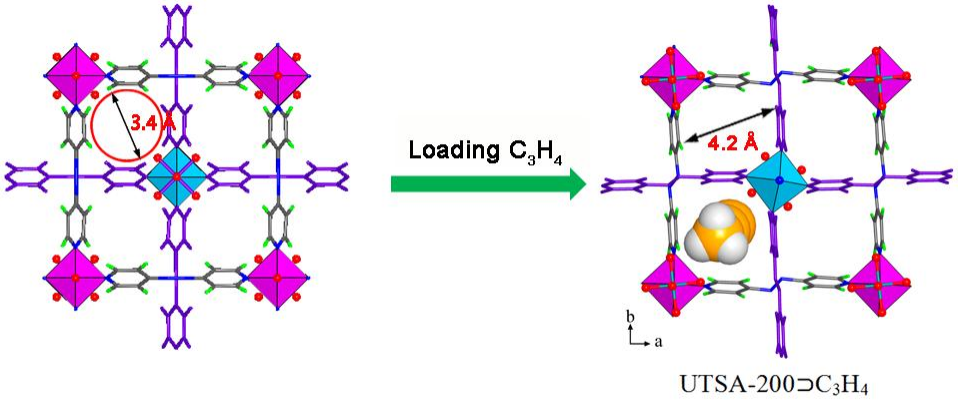

Figure S9. DFT-D-calculated C_3H_4 adsorption configuration in UTSA-200 (right structure), indicating that the N=N bond and pyridine rings on the linker would be rotated and distorted to expand the dynamic pore size from 3.4 Å to 4.2 Å after adsorbing C_3H_4 molecule. The different net is highlighted in purple for clarity. Color code: Cu (turquoise), Si (dark green), F (red), N (blue), C (grey), and H (green spheres).

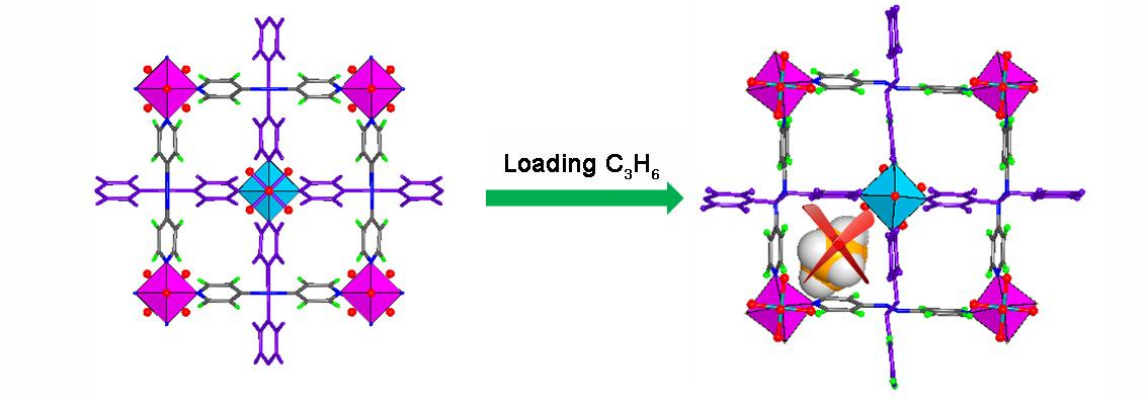

Figure S10. Hypothetical C_3H_6 adsorption configuration in the same framework model with UTSA-200⊃C_3H_4 (right structure). It is revealed that the C_3H_6 molecule would have inevitable space overlapping with the pore walls of UTSA-200, indicating that the pore needs to be expanded more for the passage of C_3H_6 molecule.

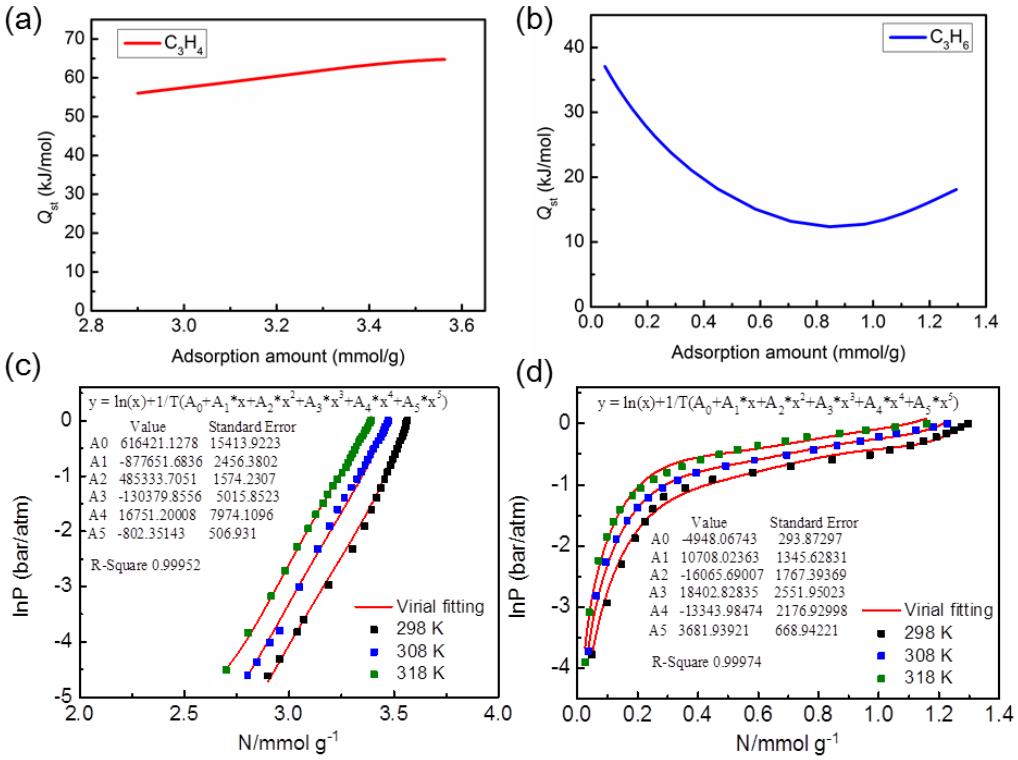

Figure S11. Adsorption heat and Virial fitting of the C_3H_4 (a and c) and C_3H_6 (b and d) adsorption isotherms for UTSA-200 (points) at 298 K (black), 308 K (blue), and 318 K (green).

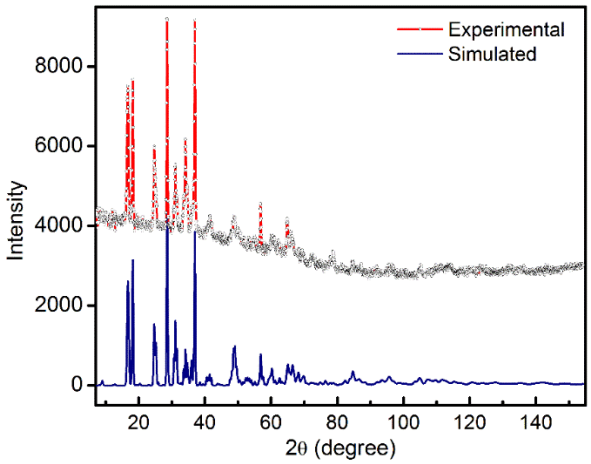

Figure S12. Neutron powder diffraction pattern of the C_3D_4-loaded UTSA-200 along with the simulated pattern based on a model structure built upon the DFT-D calculation results. The agreement between the two is reasonably well..

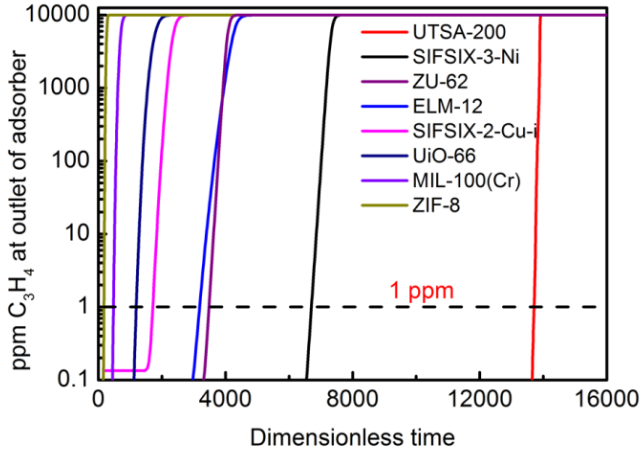

Figure S13. Ppm C_3H_4 in the outlet gas of transient breakthrough of C_3H_4/C_3H_6 mixture containing 1% C_3H_4 mixture in an adsorber bed packed with various MOFs. At a certain time, τ_{break}, the impurity level will exceed the desired purity level of 1 ppm.

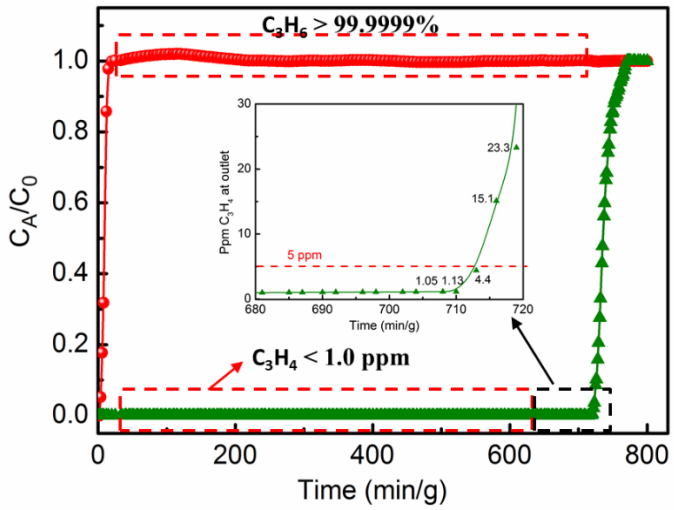

Figure S14. The concentration of C_3H_4 and the purity of C_3H_6 in the outlet gas of the adsorber. The inserted figure shows the C_3H_4 content in the outlet gas in ppm. Experimental breakthrough was conducted on a stainless steel column packed with UTSA-200 (Φ 4×150 mm) with C_3H_4/C_3H_6 mixture (1/99) as feed gas at 2.0 mL/min and 298 K.

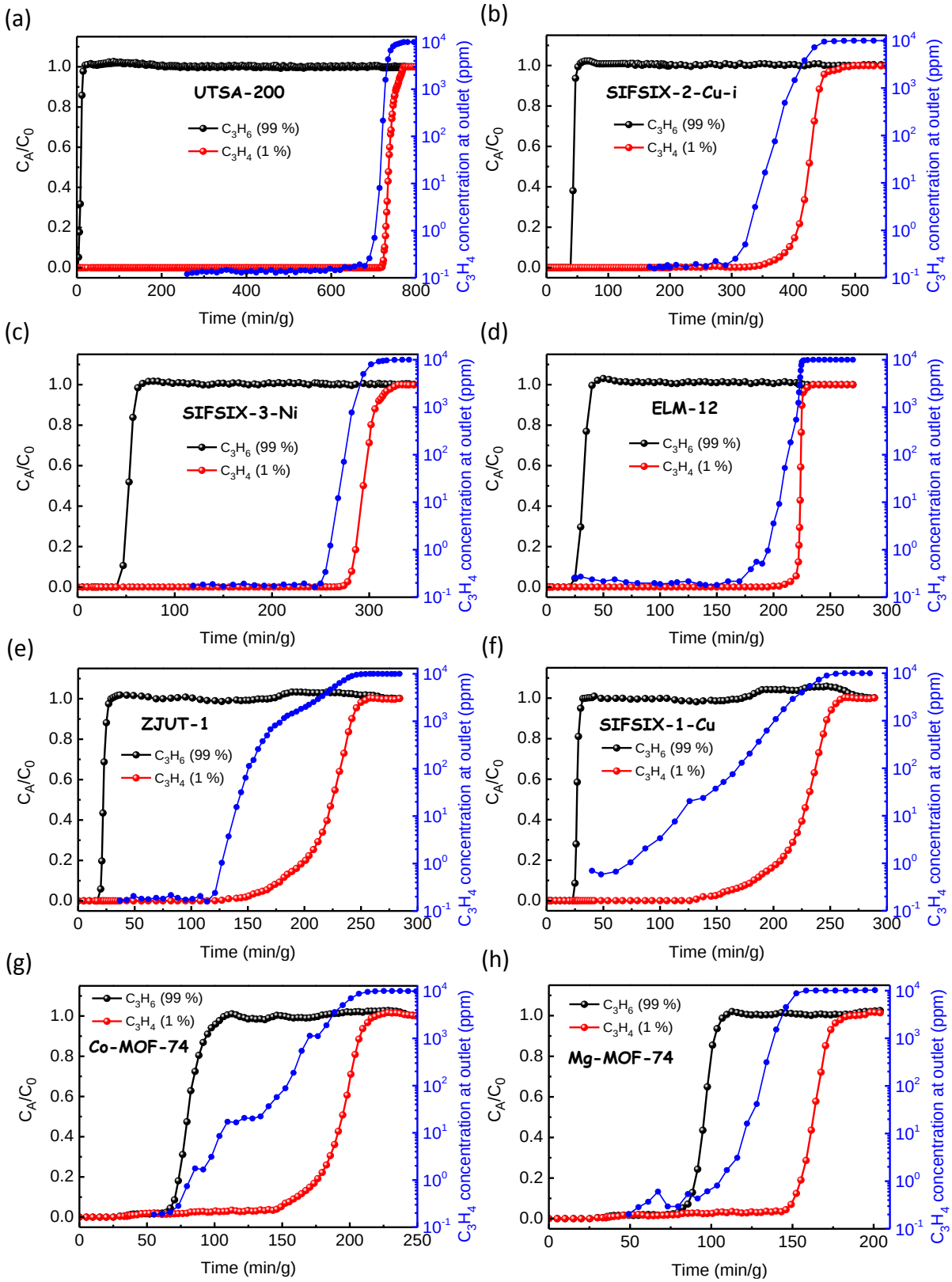
(a)
UTSA-200
(b)
SIFSIX-2-Cu-i
(c)
SIFSIX-3-Ni
(d)
ELM-12
(e)
ZJUT-1
(f)
SIFSIX-1-Cu
(g)
Co-MOF-74
(h)
Mg-MOF-74
C3H6 (99 %)
C3H4 (1 %)
CA/C0
C3H4 concentration at outlet (ppm)
Time (min/g)

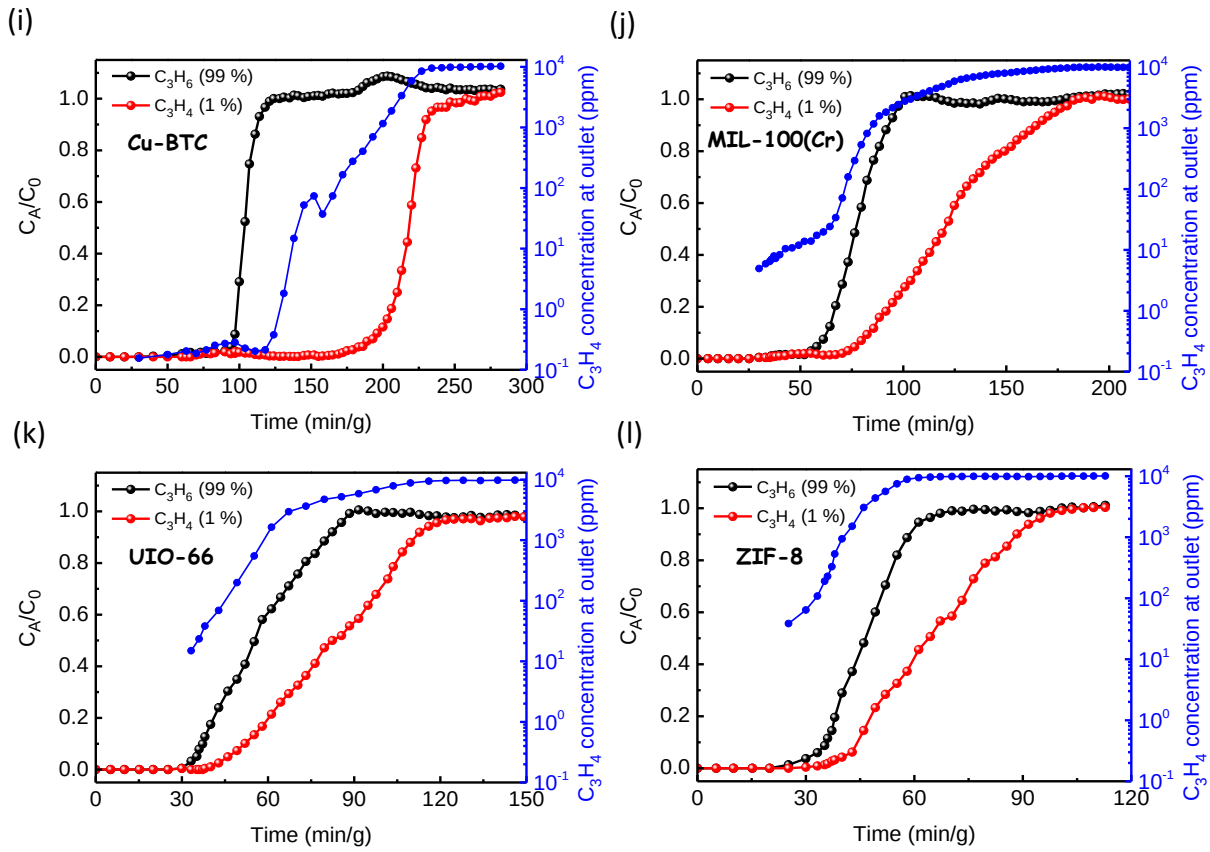

Figure S15. Breakthrough curves of the selected MOFs for separation of C_3H_4/C_3H_6 (1/99) mixtures at 298 K and 1.01 bar. Most traditional MOFs cannot meet the requirement for removal low concentration of C_3H_4 (< 1 ppm) from C_3H_4/C_3H_6 (1/99) mixtures.

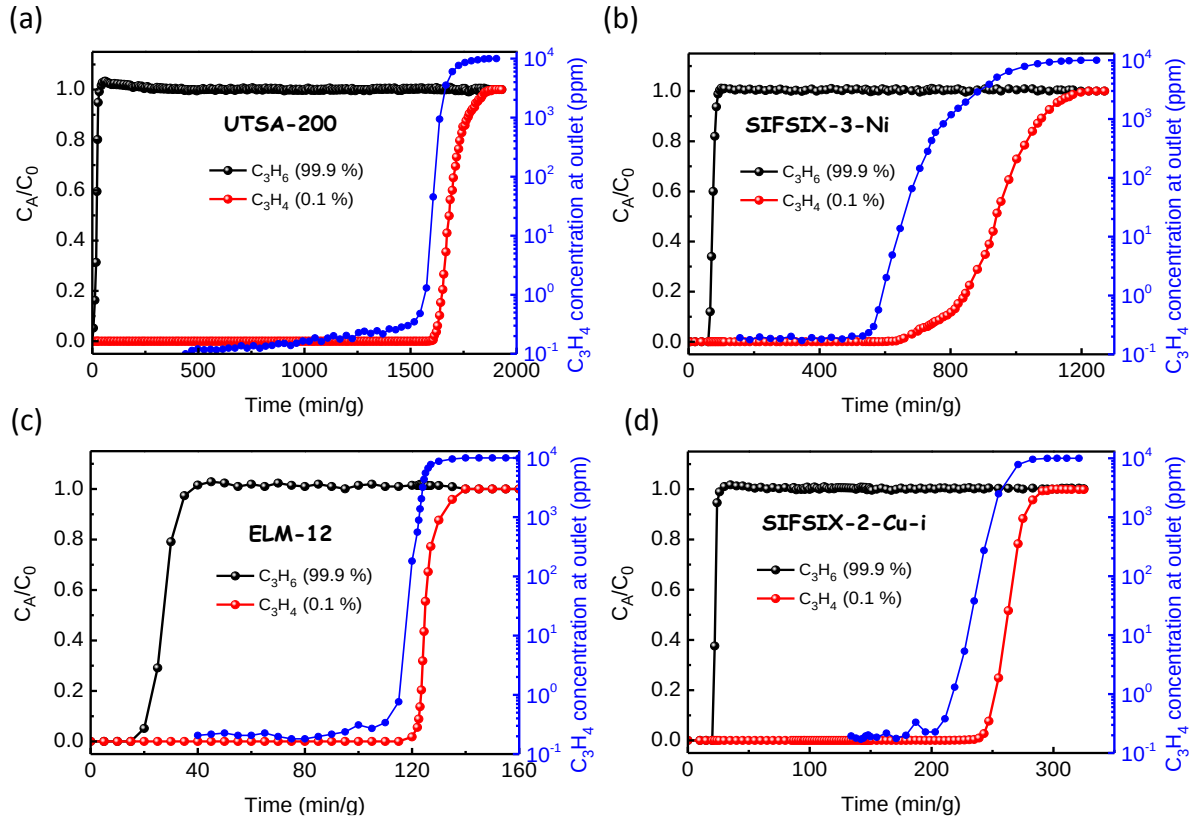

Figure S16. Breakthrough curves of the selected MOFs for separation of C_3H_4/C_3H_6 (0.1/99.9) mixture at 298 K and 1.01 bar. These indicated MOFs can remove trace C_3H_4 from C_3H_4/C_3H_6 (0.1/99.9) mixtures to meet the requirement of C_3H_4< 1 ppm.

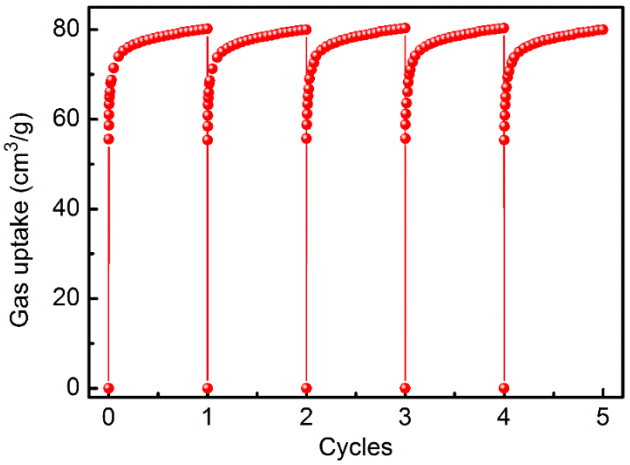

Figure S17. Cyclic C_3H_4 adsorption measurements on UTSA-200 at 298 K and 1 bar, indicating that UTSA-200 can maintain its high C_3H_4 uptake capacity over five cycles.

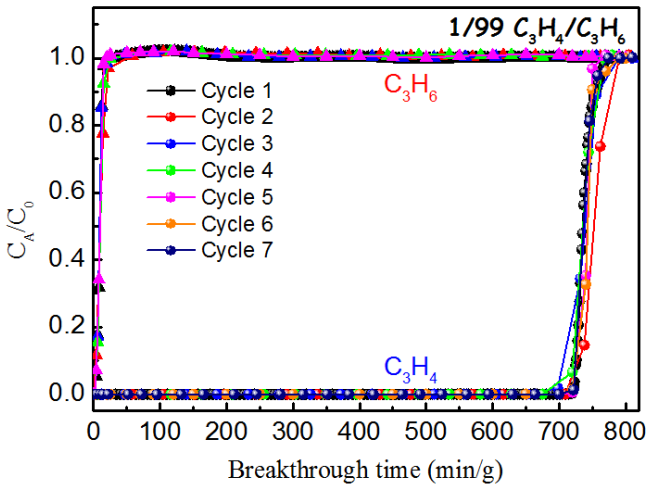

Figure S18. Cycling column breakthrough curves for C_3H_4/C_3H_6 (1/99) separations with UTSA-200 at 298 K and 1.01 bar. The breakthrough experiments were carried out in a column packed with UTSA-200 (Φ 4×150 mm) at a flow rate of 2.0 mL/min.

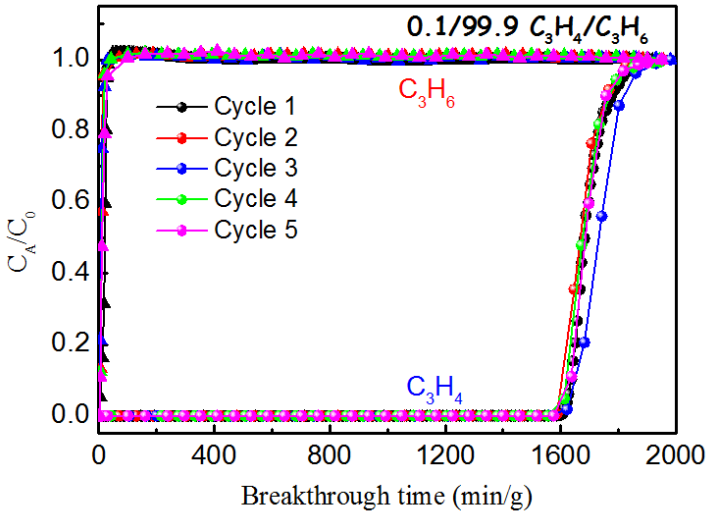

Figure S19. Cycling column breakthrough curves for C_3H_4/C_3H_6 (0.1/99.9) separations with UTSA-200 at 298 K and 1.01 bar. The breakthrough experiments were carried out in a column packed with UTSA-200 (Φ 4×150 mm) at a flow rate of 2.0 mL/min.

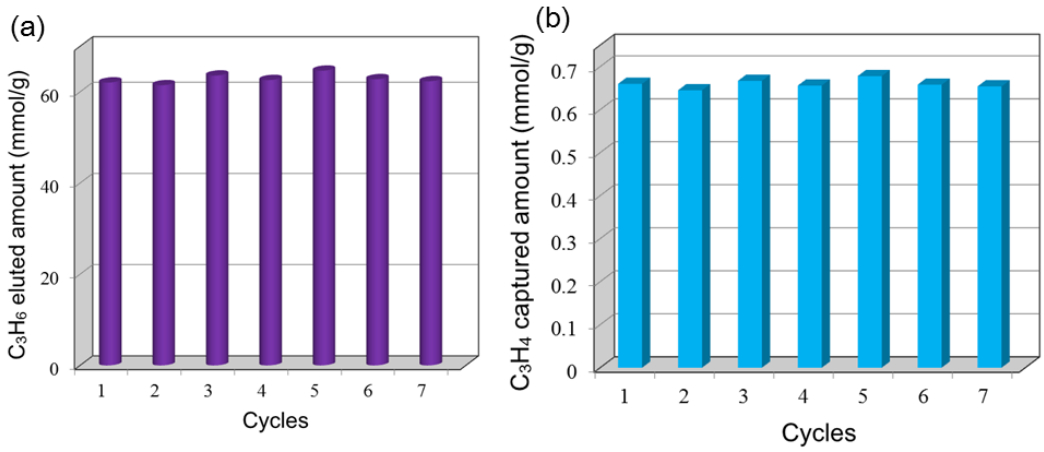

Figure S20. Cyclic breakthrough experiments for C_3H_4/C_3H_6 (1/99 v/v) separation on UTSA-200, indicating that UTSA-200 maintained the C_3H_6 eluted amount from the outlet effluent (a) and the C_3H_4 captured amount (b) during the separation processes over at least 7 times.

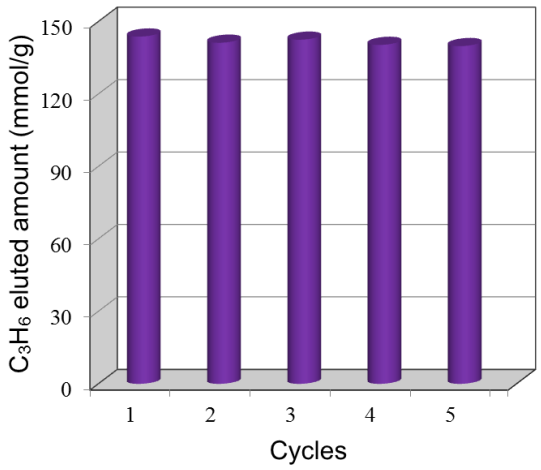

Figure S21. Cyclic breakthrough experiments for C_3H_4/C_3H_6 (0.1/99.9) separation on UTSA-200, indicating that UTSA-200 maintained the C_3H_6 eluted amount during the separation processes over at least 7 times.

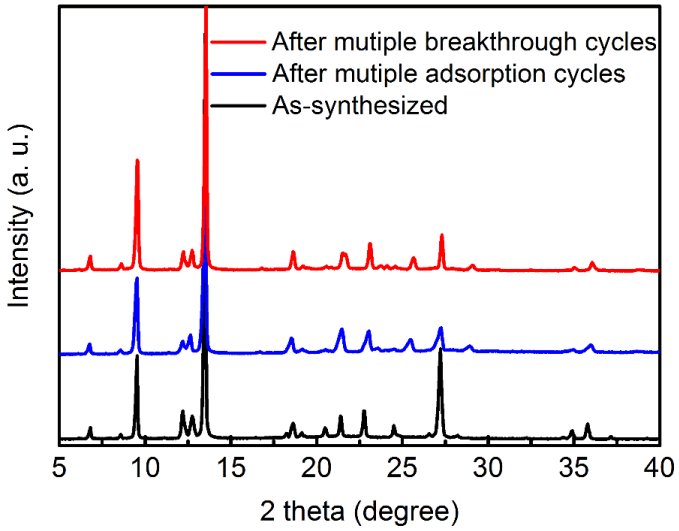

Figure S22. PXRD patterns of as-synthesized UTSA-200 sample (black) and the samples after the multiple adsorption tests (blue) and breakthrough tests (red).

SUPPORTING INFORMATION

Table S1. The BET surface, pore size and crystal density of the selected MOF materials.

MOF Types	Materials	BET surface (m^2/g)	Pore size (Å)	Crystal density (g/cm^3)	Ref.
MOFs with open metal sites	Mg-MOF-74	1415	11	0.920	[8]
	Co-MOF-74	1080	11	1.169	[8]
	Ni-MOF-74	1070	11	1.203	[8]
	Fe-MOF-74	1360	11	1.126	[9]
	UTSA-74	830	8	1.340	[10]
	Cu-BTC	1850	7-10	0.879	[11]
	Cr-BTC	1810	7-10	0.799	[12]
MOFs with high porosities	Fe-BTT	2200	10.3	0.797	[13]
	Cr-BTT	2293	10.3	0.832	[14]
	MIL-100(Cr)	3100	29	0.784	[15]
	MIL-100(Fe)	2800	32	1.064	[16]
Small-pore MOFs	UIO-66	1390	6	1.198	[17]
	ZIF-8	1630	3.5	1.067	[18]
	UTSA-100	970	4.0	1.146	[19]
	ZJUT-1	222	3.7	1.738	[20]
MOFs with strong functional sites	SIFSIX-1-Cu	1178	8.0	0.864	[21]
	SIFSIX-2-Cu-i	735	4.4	1.247	[22]
	SIFSIX-3-Ni	250	4.2	1.570	[23]
	UTSA-200	612	3.4	1.417	[24]
	ELM-12	740	4.3	1.406	[25]
	ZU-62	476	3.2	1.378	[26]

Note: the crystal density of UTSA-200 used for the unit conversion is based on the activated framework. Although the structure of UTSA-200 would be changed upon gas adsorption (mainly originated from the rotation of pyridine rings), this change is very tiny that would have a negligible impact on the crystal density, as supported by the very similar cell parameters between the activated UTSA-200 (a = b = 13.0469, c = 7.9013; $\alpha = \beta = \gamma = 90.00$)[24] and UTSA-200⊃$C_3H_4$ model (a = b = 13.0600, c = 8.0680; $\alpha = \beta = \gamma = 90.00$).

Table S2. Comparison of C_3H_4 and C_3H_6 uptake (mmol/g, mmol/cm^3 and cm^3/cm^3) from gas adsorption isotherms at various pressures, and the C_3H_4/C_3H_6 uptake ratio at 0.01/0.01 bar and 0.01/0.99 bar for various MOF materials at 298 K.

MOFs	C_3H_4 adsorption (mmol g^{-1}/mmol cm^{-3}/cm^3 cm^{-3})			C_3H_6 adsorption (mmol g^{-1}/mmol cm^{-3}/cm^3 cm^{-3})			C_3H_4/C_3H_6 adsorption ratio	
	0.01 bar	0.1 bar	0.99 bar	0.01 bar	0.4 bar	0.99 bar	0.01/0.01	0.01/0.99
UTSA-200	**2.99/4.24/95**	**3.30/4.68/105**	**3.58/5.07/114**	**0.02/0.03/0.67**	**0.33/0.47/10.5**	**1.20/1.70/38.0**	**149.5**	**2.49**
SIFSIX-3-Ni	2.56/4.02/90	2.73/4.29/96	2.85/4.47/100	0.15/0.24/5.3	2.42/3.80/85.1	2.72/4.27/95.6	17.87	0.98
ZU-62	2.19/3.02/68	3.01/4.15/93	3.64/5.02/112	0.17/0.23/5.2	2.26/3.11/69.7	2.67/3.68/82.4	12.9	0.82
SIFSIX-2-Cu-i	1.96/2.44/55	3.22/4.01/90	3.77/4.70/105	0.15/0.19/4.3	2.19/2.73/61.2	2.63/3.28/73.5	13.07	0.74
SIFSIX-1-Cu	2.57/2.22/50	6.79/5.87/131	8.63/7.46/167	0.30/0.26/5.8	4.92/4.25/95.2	5.88/5.08/113.8	8.54	0.44
ELM-12	1.82/2.56/57	2.54/3.57/80	2.77/3.89/87	0.19/0.27/6.0	1.11/1.56/35.0	1.43/2.01/45.0	9.57	1.27
ZJUT-1	0.40/0.69/15	1.07/1.86/42	2.24/3.89/87	0.06/0.10/2.24	0.54/0.94/21.0	0.84/1.46/32.7	6.67	0.47
Mg-MOF-74	2.71/2.49/56	7.32/6.73/151	9.40/8.65/194	2.03/1.87/41.9	6.07/5.58/125.0	6.49/5.97/133.7	1.33	0.42
Co-MOF-74	2.85/3.33/75	5.80/6.78/152	7.47/8.73/196	1.27/1.48/33.2	5.64/6.59/147.6	5.95/6.96/155.9	2.24	0.48
Ni-MOF-74	1.80/2.16/48	4.68/5.63/126	5.51/6.63/149	1.53/1.84/41.2	4.50/5.41/121.2	4.78/5.75/128.8	1.18	0.38
Fe-MOF-74	2.18/2.45/55	6.67/7.51/168	7.94/8.94/200	1.67/1.88/42.1	6.25/7.04/157.7	6.63/7.47/167.3	1.31	0.33
Cu-BTC	1.47/1.29/29	8.17/7.18/161	10.47/9.20/206	1.36/1.19/26.7	7.90/6.94/155.4	8.33/7.32/164.0	1.08	0.18
Fe-BTT	1.74/1.32/30	6.87/5.20/117	12.41/9.39/210	1.52/1.15/25.8	8.03/6.08/136.2	8.74/6.62/148.3	1.14	0.20
Cr-BTT	1.08/0.82/18	4.42/3.34/75	7.28/5.51/123	0.76/0.58/13.0	5.04/3.81/85.3	5.85/4.43/99.2	1.42	0.18
MIL-100(Cr)	1.52/1.11/25	4.98/3.64/82	14.51/10.62/238	0.63/0.46/10.3	4.53/3.32/74.4	6.25/4.58/102.6	2.41	0.24
MIL-100(Fe)	1.34/0.98/22	4.74/3.47/78	17.14/12.55/281	0.52/0.38/8.5	4.52/3.31/74.1	6.96/5.09/114.0	2.58	0.19
UIO-66	1.58/1.89/42	5.29/6.34/142	10.23/12.26/275	0.36/0.43/9.6	2.70/3.23/72.3	3.33/3.99/89.4	4.39	0.47
ZIF-8	0.13/0.14/3.1	1.44/1.54/35	6.27/6.69/150	0.08/0.09/2.0	3.15/3.36/75.3	4.07/4.34/97.2	1.62	0.03
UTSA-74-Zn	0.33/0.44/9.8	2.13/2.85/64	7.43/9.96/223	0.09/0.12/2.7	2.47/3.31/74.1	5.07/6.79/152.1	3.67	0.06
UTSA-100	1.87/2.14/48	4.01/4.59/103	5.35/6.13/137	1.34/1.54/34.5	2.68/3.07/68.8	3.04/3.48/77.9	1.40	0.62

Table S3. Dual-Langmuir-Freundlich fitting parameters for C_3H_4, and C_3H_6 in UTSA-200.

	Site A				Site B			
	$q_{A,sat}$ mol kg^{-1}	b_{A0} $Pa^{-\nu_i}$	E_A kJ mol^{-1}	ν_A dimensionless	$q_{B,sat}$ mol kg^{-1}	b_{B0} $Pa^{-\nu_i}$	E_B kJ mol^{-1}	ν_B dimensionless
C_3H_4	0.8	2.53E-14	56	1	2.8	4.36E-07	30.6	1
C_3H_6	1.9	1.91E-15	17	0.33	1.56	2.49E-28	92	2.44

Table S4. Dual-Langmuir-Freundlich fitting parameters for C_3H_4, and C_3H_6 in SIFSIX-3-Ni.

	Site A				Site B			
	$q_{A,sat}$ mol kg^{-1}	b_{A0} $Pa^{-\nu_i}$	E_A kJ mol^{-1}	ν_A dimensionless	$q_{B,sat}$ mol kg^{-1}	b_{B0} $Pa^{-\nu_i}$	E_B kJ mol^{-1}	ν_B dimensionless
C_3H_4	0.6	6.72E-08	27	0.42	2.65	2.52E-12	48	2
C_3H_6	2.8	2.71E-13	43	1.27	0.12	3.42E-05	49	1

Table S5. Dual-Langmuir-Freundlich fitting parameters for C_3H_4, and C_3H_6 in SIFSIX-2-Cu-i.

	Site A				Site B			
	$q_{A,sat}$ mol kg^{-1}	b_{A0} $Pa^{-\nu_i}$	E_A kJ mol^{-1}	ν_A dimensionless	$q_{B,sat}$ mol kg^{-1}	b_{B0} $Pa^{-\nu_i}$	E_B kJ mol^{-1}	ν_B dimensionless
C_3H_4	3.9	1.18E-05	10.3	1.08	2.1	1.01E-07	23.2	0.5
C_3H_6	2.2	4.63E-10	32	1	1.8	6.76E-12	36	1

Table S6. Dual-Langmuir-Freundlich fitting parameters for C_3H_4, and C_3H_6 in ELM-12.

	Site A				Site B			
	$q_{A,sat}$ mol kg^{-1}	b_{A0} $Pa^{-\nu_i}$	E_A kJ mol^{-1}	ν_A dimensionless	$q_{B,sat}$ mol kg^{-1}	b_{B0} $Pa^{-\nu_i}$	E_B kJ mol^{-1}	ν_B dimensionless
C_3H_4	2.2	2.07E-05	5	1.45	1.2	4.47E-12	52	0.45
C_3H_6	1.5	6.62E-12	36	1	0.6	1.46E-6	14	1

Table S7. Dual-Langmuir-Freundlich fitting parameters for C_3H_4 and C_3H_6 in SIFSIX-1-Cu.

	Site A			Site B		
	$q_{A,sat}$ mol kg^{-1}	b_A $Pa^{-\nu_i}$	ν_A dimensionless	$q_{B,sat}$ mol kg^{-1}	b_B $Pa^{-\nu_i}$	ν_B dimensionless
C_3H_4	6.6	2.21E-02	0.39	4.2	1.54E-6	2
C_3H_6	5.7	2.76E-3	0.5	2.9	7.43E-13	3.2

Table S8. Dual-Langmuir-Freundlich fitting parameters for C_3H_4 and C_3H_6 in UIO-66.

	Site A				Site B			
	$q_{A,sat}$ mol kg^{-1}	b_{A0} $Pa^{-\nu_i}$	E_A kJ mol^{-1}	ν_A dimensionless	$q_{B,sat}$ mol kg^{-1}	b_{B0} $Pa^{-\nu_i}$	E_B kJ mol^{-1}	ν_B dimensionless
C_3H_4	8	2.02E-08	19	1	3.8	1.01E-06	15	1
C_3H_6	2.5	9.13E-11	35.5	1	2.3	2.70E-11	31	1

Table S9. Dual-Langmuir-Freundlich fitting for C_3H_4 and C_3H_6 in MIL-100(Cr).

	Site A				Site B			
	$q_{A,sat}$ mol kg^{-1}	b_{A0} $Pa^{-\nu_i}$	E_A kJ mol^{-1}	ν_A dimensionless	$q_{B,sat}$ mol kg^{-1}	b_{B0} $Pa^{-\nu_i}$	E_B kJ mol^{-1}	ν_B dimensionless
C_3H_4	18.5	4.19E-08	15.7	1	1.7	4.52E-07	20	1
C_3H_6	8.2	2.95E-10	27	1	1.3	4.25E-08	25	1

Table S10. Dual-Langmuir-Freundlich fitting parameters for C_3H_4 and C_3H_6 in ZIF-8.

	Site A				Site B			
	$q_{A,sat}$ mol kg^{-1}	b_{A0} $Pa^{-\nu_i}$	E_A kJ mol^{-1}	ν_A dimensionless	$q_{B,sat}$ mol kg^{-1}	b_{B0} $Pa^{-\nu_i}$	E_B kJ mol^{-1}	ν_B dimensionless
C_3H_4	5.9	1.47E-10	28.6	1	3	1.59E-15	41	1.8
C_3H_6	4.9	2.28E-13	38	1.35	0.3	6.00E-19	29	0.75

Table S11. Dual-Langmuir-Freundlich fitting parameters for C_3H_4 and C_3H_6 in Cu-BTC.

	Site A				Site B			
	$q_{A,sat}$ mol kg^{-1}	b_{A0} $Pa^{-\nu_i}$	E_A kJ mol^{-1}	ν_A dimensionless	$q_{B,sat}$ mol kg^{-1}	b_{B0} $Pa^{-\nu_i}$	E_B kJ mol^{-1}	ν_B dimensionless
C_3H_4	20	4.55E-04	7.2	0.44	5.5	9.58E-11	23	2
C_3H_6	1.4	4.81E-12	36	1	8.7	2.79E-08	27	1

Table S12. Breakthrough calculations for separation of C_3H_4/C_3H_6 (1/99) mixture at 298 K.

	Separation potential ΔQ (mol/L)	Breakthrough productivity of C_3H_6 (mol/L)
UTSA-200	**404.5**	**367.2**
SIFSIX-3-Ni	210.1	182.2
ZU-62	118.9	92.8
SIFSIX-2-Cu-i	64.8	47.7
ELM-12	121.2	92.2
Cu-BTC	18.7	/
MIL-100(Cr)	15.8	9.9
UIO-66	47.4	31.8
ZIF-8	3.6	1.6

Table S13. Comparisons of the breakthrough columns parameters studied in this work.

	Sample weight (g)	Crystal density (g/cm^3)	Packing density[a] (g/cm^3)	Column voidage[b]	Column free space (cm^3)[c]
UTSA-200	**2.028**	**1.417**	**1.152**	**0.187**	**0.329**
SIFSIX-3-Ni	2.411	1.570	1.430	0.192	0.338
SIFSIX-2-Cu-i	2.054	1.247	1.167	0.180	0.317
ELM-12	2.017	1.406	1.146	0.185	0.326
ZJUT-1	2.360	1.738	1.401	0.194	0.341
Cu-BTC	1.197	0.879	0.692	0.213	0.375
Co-MOF-74	1.466	1.169	0.927	0.207	0.364
Mg-MOF-74	1.302	0.920	0.740	0.195	0.342
SIFSIX-1-Cu	1.258	0.864	0.706	0.183	0.322
MIL-100(Cr)	1.034	0.732	0.588	0.196	0.345
UIO-66	1.723	1.198	0.979	0.183	0.322
ZIF-8	1.387	1.067	0.830	0.222	0.391

[a] Packing density = Sample weight/Column volume

[b] Column voidage = 1- Sample weight/Crystal density/Column volume

[c] Column free space = Column volume × Column voidage

Table S14. Comparisons of C_3H_6 productivities in a single breakthrough operation using C_3H_4/C_3H_6 (1/99) mixture as input.

	Crystal density (g/cm^3)	Gravimetric/Volumetric Productivity (mmol/g and $mmol/cm^3$) with different purities	
		C_3H_6 (C_3H_4 < 1 ppm)	C_3H_6 (C_3H_4 < 5 ppm)
UTSA-200	**1.417**	**62.05 / 87.92**	**62.94 / 89.19**
SIFSIX-3-Ni	1.570	19.02 / 33.66	19.60 / 34.69
SIFSIX-2-Cu-i	1.247	26.34 / 37.48	27.68 / 39.39
ELM-12	1.406	15.36 / 21.60	15.80 / 22.21
ZJUT-1	1.738	17.86 / 31.04	19.28 / 33.51
Cu-BTC	0.879	2.77 / 2.43	2.91 / 2.56
Co-MOF-74	1.169	2.11 / 2.47	2.32 / 2.71
Mg-MOF-74	0.920	1.78 / 1.64	2.47 / 2.27
SIFSIX-1-Cu	0.864	4.46 / 3.85	6.69 / 5.78
MIL-100(Cr)	0.732	NA	NA
UIO-66	1.198	NA	NA
ZIF-8	1.067	NA	NA

Table S15. Comparisons of C_3H_6 productivities in a single breakthrough operation using C_3H_4/C_3H_6 (0.1/99.9) mixture as input.

	Crystal density (g/cm^3)	Gravimetric/Volumetric Productivity (mmol/g and $mmol/cm^3$) with different purities	
		C_3H_6 (C_3H_4 < 1 ppm)	C_3H_6 (C_3H_4 < 5 ppm)
UTSA-200	**1.417**	**142.86 / 202.43**	**143.75 / 203.69**
SIFSIX-3-Ni	1.570	47.32 / 83.76	49.11 / 86.92
SIFSIX-2-Cu-i	1.247	8.48 / 12.07	8.75 / 12.45
ELM-12	1.406	17.86 / 25.11	18.93 / 26.62

References

[1] P. Nugent, Y. Belmabkhout, S. D. Burd, A. J. Cairns, R. Luebke, K. Forrest, T. Pham, S. Ma, B. Space, L. Wojtas, M. Eddaoudi, M. J. Zaworotko, *Nature* **2013**, *495*, 80-84.

[2] X. Cui, K. Chen, H. Xing, Q. Yang, R. Krishna, Z. Bao, H. Wu, W. Zhou, X. Dong, Y. Han, B. Li, Q. Ren, M. J. Zaworotko, B. Chen, *Science* **2016**, *353*, 141-144.

[3] B. Li, X. Cui, D. O'Nolan, H.-M. Wen, M. Jiang, R. Krishna, H. Wu, R.-B. Lin, Y. S. Chen, D. Yuan, H. Xing, W. Zhou, Q. Ren, G. Qian, M. J. Zaworotko, B. Chen, *Adv. Mater.* **2017**, *29*, 1704210.

[4] O. Shekhah, Y. Belmabkhout, K. Adil, P. M. Bhatt, A. J. Cairns, M. Eddaoudi, *Chem. Commun.* **2015**, *51*, 13595-13598.

[5] D. O'Nolan, A. Kumar, M. J. Zaworotko, *J. Am. Chem. Soc.* **2017**, *139*, 8508-8513.

[6] D. O'Nolan, D. G. Madden, A. Kumar, K.-J. Chen, T. Pham, K. A. Forrest, E. Patyk-Kazmierczak, Q.-Y. Yang, C. A. Murray, C. C. Tang, B. Space, M. J. Zaworotko, *Chem. Commun.* **2018**, *54*, 3488-3491.

[7] R. Krishna, *RSC Adv.* **2017**, *7*, 35724-35737.

[8] S. R. Caskey, A. G. W.-F., A. J. Matzger, *J. Am. Chem. Soc.* **2008**, *130*, 10870-10871.

[9] E. D. Bloch, W. L. Queen, R. Krishna, J. M. Zadrozny, C. M. Brown, J. R. Long, *Science* **2012**, *335*, 1606-1610.

[10] F. Luo, C. Yan, L. Dang, R. Krishna, W. Zhou, H. Wu, X. Dong, Y. Han, T.-L. Hu, M. O'Keeffe, L. Wang, M. Luo, R.-B. Lin, B. Chen, *J. Am. Chem. Soc.* **2016**, *138*, 5678-5684.

[11] S. S. Y. Chui, S. M. F. Lo, J. P. H. Charmant, A. G. Orpen, I. D. A Williams, *Science* **1999**, *283*, 1148-1150.

[12] L. J. Murray, M. Dinca, J. Yano, S. Chavan, S. Bordiga, C. M. Brown, J. R. Long, *J. Am. Chem. Soc.* **2010**, *132*, 7856-7857.

[13] K. Sumida, S. Horike, S. S. Kaye, Z. R. Herm, W. L. Queen, C. M. Brown, F. Grandjean, G. J. Long, A. Dailly, J. R. Long, *Chem. Sci.* **2010**, *1*, 184-191.

[14] E. D. Bloch, W. L. Queen, M. R. Hudson, J. A. Mason, D. J. Xiao, L. J. Murray, R. Flacau, C. M. Brown, J. R. Long, *Angew. Chem. Int. Ed.* **2016**, *55*, 8605-8609.

[15] G. Férey, C. Serre, C. Mellot-Draznieks, F. Millange, S. Surblé, J. Dutour, I. Margiolaki, *Angew. Chem. Int. Ed.* **2004**, *43*, 6456-6461.

[16] P. Horcajada, S. Surblé, C. Serre, D.-Y. Hong, Y.-K. Seo, J.-S. Chang, J.-M. Grenéche, I. Margiolaki, G. Férey, *Chem. Commun.* **2007**, 2820-2822.

[17] J. H. Cavka, S. Jakobsen, U. Olsbye, N. Guillou, C. Lamberti, S. Bordiga, K. P. Lillerud, *J. Am. Chem. Soc.* **2008**, *130*, 13850-13851.

[18] K. S. Park, Z. Ni, A. P. Côté, J. Y. Choi, R. Huang, F. J. Uribe-Romo, H. K. Chae, M. O'Keeffe, O. M. Yaghi, *Proc. Natl. Acad. Sci.* **2006**, *103*, 10186-10191.

[19] T.-L. Hu, H. Wang, B. Li, R. Krishna, H. Wu, W. Zhou, Y. Zhao, Y. Han, X. Wang, W. Zhu, Z. Yao, S. Xiang, B. Chen, *Nat. Commun.* **2015**, *6*, 7328.

[20] H.-M. Wen, L. Li, R.-B. Lin, B. Li, B. Hu, W. Zhou, J. Hu, B. Chen, *J. Mater. Chem. A* **2018**, *6*, 6931-6937.

[21] S. D. Burd, S. Ma, J. A. Perman, B. J. Sikora, R. Q. Snurr, P. K. Thallapally, J. Tian, L. Wojtas, M. J. Zaworotko, *J. Am. Chem. Soc.* **2012**, *134*, 3663-3666.

[22] P. Nugent, Y. Belmabkhout, S. D. Burd, A. J. Cairns, R. Luebke, K. Forrest, T. Pham, S. Ma, B. Space, L. Wojtas, M. Eddaoudi, M. J. Zaworotko, *Nature* **2013**, *495*, 80-84.

[23] A. Kumar, D. G. Madden, M. Lusi, K.-J. Chen, E. A. Daniels, T. Curtin, J. J. Perry IV, M. J. Zaworotko, *Angew. Chem. Int. Ed.* **2015**, *54*, 14372-14377.

[24] B. Li, X. Cui, D. O'Nolan, H.-M. Wen, M. Jiang, R. Krishna, H. Wu, R.-B. Lin, Y. S. Chen, D. Yuan, H. Xing, W. Zhou, Q. Ren, G. Qian, M. J. Zaworotko, B. Chen, *Adv. Mater.* **2017**, *29*, 1704210.

[25] L. Li, R.-B. Lin, R. Krishna, X. Wang, B. Li, H. Wu, J. Li, W. Zhou, B. Chen, *J. Am. Chem. Soc.* **2017**, *139*, 7733-7736.

[26] L. Yang, X. Cui, Z. Zhang, Q. Yang, Z. Bao, Q. Ren, H. Xing *Angew. Chem. Int. Ed.* **2018**, *doi: 10.1002/anie.201807652.*

Author Contributions

J.L., B.L., and B.C. contributed to conceive and design the experiments. L.L., H.M.W., and B.L. synthesized the compounds and collected the gas adsorption data. L.L., R.B.L., B.L., and B.C. analyzed all adsorption data. R.K. conducted IAST calculations and transient breakthrough simulations. H.W. and W.Z. collected and analyzed the powder X-ray diffraction data. H.W. and W.Z. performed the first-principles DFT-D calculations and neutron diffraction. L.L., C.H., and B.L. collected the experimental breakthrough data. L.L., B.L., and B.C. analyzed the data and wrote the manuscript. All authors discussed the results and commented on the manuscript.